

# Design and Characterization of a Passive Wireless DNA Sensor

by

HAIBO XU

A thesis submitted in partial fulfillment of the requirements for the degree of

MASTER OF SCIENCES

In

MECHANICAL ENGINEERING

UNIVERSITY OF PUERTO RICO  
MAYAGÜEZ CAMPUS

2014

Approved by:

\_\_\_\_\_  
Manuel Toledo-Quiñones, Ph.D.  
Member, Graduate Committee

\_\_\_\_\_  
Date

\_\_\_\_\_  
Paul Sundaram, Ph.D.  
Member, Graduate Committee

\_\_\_\_\_  
Date

\_\_\_\_\_  
Yi Jia, Ph.D.  
President, Graduate Committee

\_\_\_\_\_  
Date

\_\_\_\_\_  
Marco A. De Jesús  
Representative of Graduate Study

\_\_\_\_\_  
Date

\_\_\_\_\_  
Ricky Valentín, Ph.D.  
Chairperson of the Department

\_\_\_\_\_  
Date

## ABSTRACT

In order to predict and avoid disasters due to gene mutation, reliable DNA information is necessary to be monitored in real time. Existing DNA sensing technologies offer outstanding performance in terms of the resolution and time response. However, these technologies require either physical connection of signal communication, a battery power supply or expensive equipment for acquiring DNA information. The limitations make existing DNA sensing technologies complex and hard to access.

The motivation of the proposed research is to develop an innovative DNA sensing platform which exploits a multidisciplinary area synthesizing the conventional DNA capacitive sensing mechanism and surface-based conformational characterization throughout DNA immobilization and hybridization. Compared with previous work [1], in which the capacitance measurement is fully employed, we develop another method – impedance measurement with expected features of high sensitivity, passively and wirelessly integrated. The sensor is activated by electromagnetic waves and the resonant frequency of the sensor is interrogated remotely with a single loop antenna by monitoring the frequency response of the voltage across it. The feasibility of using electrochemical impedance measurements on the proposed planar circuit to detect DNA behavior directly without chemical labels is demonstrated. The resonant frequency shift caused by the change of capacitance throughout DNA immobilization and hybridization occurring on top of a capacitor is monitored by the means of impedance analyzer, with which it is possible to inspect the graph amplitude on the behavior of signal strength and compute the quality

factor of the coupling element represented by bandwidth. In order to get a sensor with the best sensitivity, smallest size, longest detection distance and highest quality factor, the design consideration and method for the sensor together with the interdigital capacitor and the planar inductor are indicated in a posterior section. Experiments for measuring the frequency shift due to interface charge transmission were carried out in order to study its DNA sensing mechanism and possibility of DNA sensing enhancement. Finally, 32 samples were measured throughout the experiment and the average capacitance values which represented a variety of surface charge resulting from DNA molecule behavior were obtained. The capacitance changed from 11.58pF to 114.5pF when specific ssDNA was attached to electrodes and then increased to 218.6pF once complementary strand DNA was involved and hybridized with existing DNA chains. In addition, using impedance analyzer measurements, the resonant frequency decreased from 2.01MHz to 1.97MHz in the presence of ssDNA and further down to 0.95MHz since complementary strand DNA was deposited. Consequently an innovative passive wireless DNA sensor has been successfully demonstrated.

## RESUMEN

Para poder predecir y prevenir desastres causados por mutación genética, información confiable de ADN debe ser monitoreada en tiempo real. La tecnología existente ofrece una excelente ejecución en términos de resolución y respuesta. Sin embargo, estas tecnologías usualmente requieren conexión física para establecer comunicación, una fuente de potencia y equipo adicional costoso para la adquisición de información de ADN. Debido a estas limitaciones las tecnologías de detección de ADN resultan complejas y poco accesibles.

La motivación de la investigación aquí propuesta es desarrollar una plataforma de detección de ADN que de forma multidisciplinaria integre el mecanismo convencional de detección de ADN, mediante un elemento capacitivo, y un método de caracterización superficial, basado en la inmovilización e hibridación de ADN. Comparando con el trabajo previo [1], en el cual se emplea la medición de capacitancia, se desarrollo otro método, basado en la medida de impedancia, del cual se espera obtener alta sensibilidad, integrado de forma pasiva e inalámbrica. El sensor es activado por ondas electromagnéticas y luego su frecuencia de resonancia es obtenida de forma remota utilizando una antena de bobina simple y midiendo la respuesta de frecuencia para el voltaje inducido. La viabilidad de implementar la medición de impedancia electroquímica en el circuito planar propuesto para detectar el comportamiento de ADN de forma directa sin realizar una caracterización química es comprobada. El cambio en la frecuencia de resonancia causado por el cambio en la capacitancia debido a la inmovilización e hibridación de ADN en la superficie del

capacitor es monitoreado utilizando un analizador de impedancia. De esta forma es posible inspeccionar la gráfica de amplitud y calcular el factor de calidad para el elemento de acoplamiento, el cual es representado por el ancho de banda. El diseño de este sensor junto con el diseño del capacitor interdigital y el inductor planar respectivo, se realizó buscando obtener un sensor con una sensibilidad óptima, mínimo tamaño, máximo alcance y con el factor de calidad más alto posible. El método detallado de diseño es explicado en la sección posterior. Experimentos para medir el cambio en frecuencia debido a la transferencia de cargas en la interface, fueron realizados con el propósito de estudiar su mecanismo de detección de ADN y la posibilidad de mejorar los métodos de detección de ADN. Finalmente, 32 muestras fueron obtenidas a través del experimento. Analizando estas se obtuvieron los valores promedios de capacitancia, los cuales representan una variedad de cargas superficiales resultantes del comportamiento de ADN obtenido en cada caso. La capacitancia varió desde 11.58pF hasta 114.5pF. Al añadir partículas específicas de ffADN la capacitancia incrementó a 218.6pF, debido a la integración e hibridación de ADN a las cadenas existentes. En adición, utilizando medidas del analizador de impedancia, la frecuencia de resonancia disminuyó de 2.01MHz a 1.97MHz en la presencia de ffADN y redujo aún más hasta 0.95MHz al depositar material de ADN complementario. Consecuentemente, la detección de ADN es mejorada mediante el diseño de un sensor inalámbrico pasivo.

To my family . . .

## ACKNOWLEDGEMENTS

I am deeply indebted to many people who helped me in pursuing and finishing this research. Firstly, I would like to thank my thesis advisor, Professor Yi Jia, who gave me the opportunity to join his group in January, 2013. I am grateful for having been offered a chance to gain direct engineering knowledge by joining a research group where the focus is the development of novel sensors. I also feel grateful for his continuous support and encouragement that helped me overcome the disappointments that are so abundant in any experimental and theoretical problem. Finally, I must thank him for our numerous discussions on a variety of scientific, engineering, cultural, and political subjects which augmented my vision and understanding.

I would like to thank Dr. Carlos R. Cabrera and his group from UPRRP, in charge of preparing DNA molecule and arranging chemical experiments for the study of the capacitive label-free detection of DNA immobilization and hybridization process. I would like to express my special thanks to Dr. Carlos R. Cabrera for sponsoring an opportunity of summer research in Rio Piedras for the experimental part of this thesis. I would like to be grateful for Dr. Paul A. Sundaram due to his supportive encouragement as a member of my graduate committee. I also would like to express my thanks to Dr. Toledo-Quiñones for his explanation on the reader design. Last but not least, this project would not have been possible without the kind help of my co-workers Hong Li and Orlando J Lopez Vazquez.

I would also like to thank my family and girlfriend. Their love and understanding helped me through the most difficult time of this work.

The Grant from NSF 1152940 provided the funding and resources for the development of this research.

# Table of Contents

ABSTRACT .....	II
RESUMEN .....	IV
ACKNOWLEDGEMENTS.....	VII
TABLE OF CONTENTS .....	IX
LIST OF TABLES.....	XI
LIST OF FIGURES .....	XII
NOMENCLATURE .....	XIV
<b>1 INTRODUCTION .....</b>	<b>1</b>
1.1 BACKGROUND .....	1
1.2 DNA BIOLOGICAL CONCEPT .....	2
1.3 THE PROPOSED DNA SENSING SYSTEM .....	3
1.4 RESEARCH OBJECTIVE .....	4
1.5 THESIS ORGANIZATION.....	5
<b>2 LITERATURE REVIEW .....</b>	<b>7</b>
<b>3 INTERDIGITAL CAPACITANCE .....</b>	<b>11</b>
3.1 INTRODUCTION.....	11
3.2 THEORY AND CALCULATIONS.....	14
3.2.1 <i>Single semi-infinite layer capacitance</i> .....	15
3.2.2 <i>N-layer capacitance</i> .....	16
3.2.3 <i>Computation of <math>C_I(h_i)</math> and <math>C_E(h_i)</math></i> .....	18
3.3 RESULT AND DISCUSSION.....	20
3.4 FURTHER DISCUSSION .....	22
3.4.1 <i>Brief Introduction</i> .....	22
3.4.2 <i>Theory and Calculations</i> .....	23
<b>4 SELECTION OF SENSOR DESIGN .....</b>	<b>26</b>
4.1 DNA SENSING PRINCIPLES .....	26
4.2 SELECTION OF CAPACITOR DESIGN.....	28
4.2.1 <i>IDC-S with top air layer</i> .....	29
4.2.2 <i>IDC-S with one sensitive layer</i> .....	32
4.3 DESIGN OF SPIRAL INDUCTOR.....	37
4.4 SENSOR PERFORMANCE .....	40
4.4.1 <i>Electrical Model of Resonant Circuit</i> .....	40
4.4.2 <i>Q Factor</i> .....	47
4.4.3 <i>Coupling Factor</i> .....	48
4.5 CONCLUSIONS.....	51
<b>5 SENSOR CHARACTERIZATIONS .....</b>	<b>52</b>
5.1 EXPERIMENT PREPARATION.....	52
5.1.1 <i>Impedance Principles</i> .....	52

5.1.2	<i>Experiment Materials</i> .....	54
5.1.3	<i>Equipment and Instrumentation</i> .....	55
5.1.4	<i>Interdigital Array Microelectrode Preparation</i> .....	56
5.1.5	<i>Preparation of DNA</i> .....	57
5.1.6	<i>Proposed Antenna Arrangement for the Impedance Analyzer</i> .....	58
5.2	EXPERIMENT SETUP .....	59
5.2.1	<i>Dummy Test</i> .....	59
5.2.2	<i>Actual Measuring Test Setup</i> .....	61
5.3	SENSOR PERFORMANCES CHARACTERIZATION .....	63
5.3.1	<i>Experiment Procedure</i> .....	63
5.3.2	<i>Experiment Result</i> .....	65
5.3.2.1	Clean IDC capacitance Result .....	65
5.3.2.2	Immobilization of ssDNA .....	67
5.3.2.3	Hybridization of the Complementary Strand.....	68
5.3.3	<i>Result discussion</i> .....	70
<b>6</b>	<b>CONCLUSIONS AND FUTURE WORK</b> .....	<b>74</b>
6.1	CONCLUSION .....	74
6.2	FUTURE WORK .....	75
	<b>REFERENCES</b> .....	<b>77</b>
	<b>APPENDIX A. NOVEL PLANAR INDUCTOR</b> .....	<b>85</b>
A.1	THE ANALYTICAL CALCULATION OF PLANAR INDUCTOR.....	85
A.1.1	<i>Self Inductance</i> .....	89
A.1.2	<i>Mutual Inductance</i> .....	90
A.1.3	<i>Algorithm for Multi-wire Coils</i> .....	91
A.2	PROOF OF CONCEPT OF THE ANTENNA WITH NOVEL CONFIGURATION .....	92
A.3	CONCLUSIONS.....	96
	<b>APPENDIX B. SENSOR FABRICATION</b> .....	<b>97</b>
B.1	PATTERN DESIGN .....	97
B.2	FABRICATION PROCEDURE.....	99

# List of Tables

<b>Tables</b>	<b>Page</b>
Table 3.1 Detailed equations needed for the calculation of $C_E$ and $C_I$ for PPC case [44]	19
Table 3.2 Detailed equations for the calculation of $C_E$ and $C_I$ for SPC case [44] .....	25
Table 4.1 The geometrical parameters of the proposed capacitor .....	36
Table 4.2 System Parameter Values .....	46
Table 5.1 Capacitance Change after each Experimental Stage.....	71
Table 5.2 RF Change after each Experimental Stage .....	71
Table B.0.1 Fabrication parameter.....	99

# List of Figures

Figures	Page
Fig 1.1 Structure of DNA from U.S National Library of Medicine .....	3
Fig 1.2 The proposed wireless sensor scheme .....	4
Fig 2.1 On the left, the steps involved in the detection of a specific DNA sequence using an electrochemical DNA hybridization sensor. On the right, a scheme showing one of the modifications involved in this research, the indirect modification, during the detection of a specific DNA sequence [5]. .....	7
Fig 3.1 (a) Layout of electrode plane; (b) Cross-section of a periodic IDC-S.....	12
Fig 3.2 Unit cell model of the proposed multi-layered interdigital capacitor.....	13
Fig 3.3 Schematic of the equivalent circuit for evaluation of the static capacitance of a semi-infinite top layer in a periodic IDC-S with N electrodes. ....	15
Fig 3.4 Splitting of a N-layered plane according to the partial capacitance technique. ...	17
Fig 3.5 Capacitance as a function of $\eta$ and $r$ .....	22
Fig 4.1 Methods for immobilizing different biomolecules onto electrode surfaces [53].	27
Fig 4.2 Tendency of the equivalent capacitances for DNA immobilization and hybridization [54]......	28
Fig 4.3 Dependence of capacitance on $h_s$ with top air layer .....	30
Fig 4.4 Dependence of capacitance on $\eta$ with different $r$ .....	31
Fig 4.5 Dependence of capacitance on $h_s$ with one sensitive layer .....	33
Fig 4.6 Dependence of capacitance on geometric parameter $r$ .....	34
Fig 4.7 Dependence of capacitance on permittivity of sensitive layer .....	35
Fig 4.8 Layout of interdigital capacitor sensing element.....	37
Fig 4.9 Schematic of Spiral Inductor .....	38
Fig 4.10 Inductance vs. Coil Mean Radius.....	39
Fig 4.11 Inductively Coupled Circuit .....	41
Fig 4.12 Magnitude & Phase Angle of $Z_0$ .....	45
Fig 4.13 Q-factor vs. Resistance & Inductance .....	48
Fig 4.14 Coupling factor vs. Length of radius of sensor, $r_s$ (cm), with different $r_R$ .....	50
Fig 4.15 Radius of the sensor inductor design result.....	50
Fig 4.16 The home made inductor .....	51
Fig 5.1 Vector plane with imaginary part (X) and real part (R) [13].....	53
Fig 5.2 Impedance measurement vector plane representation of a.....	54
Fig 5.3 Agilent 4396B setup with impedance test kit Agilent 43961A .....	56
Fig 5.4 Agilent 4285A Precision LCR meter.....	56
Fig 5.5 Cyclic Voltammogram for $3\mu\text{m}$ IDA Au electrode in 0.5 M $\text{H}_2\text{SO}_4$ at 100 mV/s .....	57
Fig 5.6 DNA sample preparation process [21] .....	58

Fig 5.7 Impedance test antenna arrangement.....	59
Fig 5.8 Experimental setup.....	59
Fig 5.9 The resonant frequency versus the known-value capacitance.....	60
Fig 5.10 Sensor calibration setup with network analyzer.....	61
Fig 5.11 Sensor calibration setup with LCR meter.....	62
Fig 5.12 Baseline measurement.....	63
Fig 5.13 Measurement with bare electrodes.....	64
Fig 5.14 Preparation of ssDNA for immobilization.....	64
Fig 5.15 Clean IDAM capacitance in air.....	65
Fig 5.16 The impedance of bare clean electrodes.....	66
Fig 5.17 Clean IDAM capacitance in MES buffer solution.....	66
Fig 5.18 IDAM capacitance after ssDNA immobilization.....	67
Fig 5.19 The impedance measurement after ssDNA immobilization.....	68
Fig 5.20 The blank measurement after non-complementary strand.....	68
Fig 5.21 IDAM capacitance after dsDNA hybridization.....	69
Fig 5.22 The impedance measurement after complementary strand.....	69
Fig 5.23 The capacitance measurement after each experiment stage.....	70
Fig 5.24 The impedance measurement after each experiment stage.....	71
Fig 5.25 Capacitance measured with or without buffer.....	72
Fig A.0.1 Conventional spiral inductor.....	85
Fig A.0.2 Layout of multi turns square planar inductor.....	86
Fig A.0.3 (a) Magnetic flux density B at point (x, y) arising from a current I and (b) Coil with two turns [48].....	88
Fig A.0.4 Parallel square shape antenna configuration.....	93
Fig A.0.5 Experiment setup with seven coil turns.....	94
Fig A.0.6 Experiment setup with five coil turns.....	94
Fig A.0.7 Experiment setup with three coil turns.....	94
Fig A.0.8 Experiment setup with one coil turns.....	95
Fig A.0.9 Number of inductance turns VS. Frequency Peak.....	95
Fig B.0.1 Two chips on top of silicon wafer substrate.....	98
Fig B.0.2 Sensor fabrication procedure.....	101
Fig B.0.3 Fabricated sensor prototype.....	101

## NOMENCLATURE

Symbol	Unit	Name
A	mm <sup>2</sup>	Sensing area of the sensor
a	mm	Coil wire radius
C <sub>R</sub>	F	Capacitance of the reader
C <sub>S</sub>	F	Capacitance of the sensor
G	mm	Gaps between electrodes
W	mm	Width of each fingers
$\lambda$	mm	Spatial sensor wavelength
$\epsilon_0$	F/m	Permittivity of free space $8.85 \times 10^{-12}$
$\epsilon$	/	Relative permittivity value
$\eta$	/	Metal ratio
f <sub>r</sub>	Hz	Resonant frequency
I <sub>1</sub>	mA	Current on the reader antenna
I <sub>2</sub>	mA	Current on the sensor
k	/	Coupling Coefficient
L <sub>R</sub>	mH	Inductance of the reader
L <sub>S</sub>	mH	Inductance of the sensor
M	mH	Mutual inductance
n	/	Turns of the coil
Z	Ohm	Impedance

$R_s$	Ohm	Self resistance of the sensor
$\mu_0$	H/m	Magnetic permeability of free space $4 \pi \times 10^{-7}$
$r_R$	mm	Radius of the primary coil
$r_S$	mm	Radius of the sensor inductor
$D$	mm	Coupling distance
PPC	/	Parallel partial capacitance
SPC	/	Serial partial capacitance
DNA	/	Deoxyribose nucleic Acid
ssDNA	/	Single strand DNA
dsDNA	/	Double strand DNA
SAM	/	Self-assembled monolayer
RNA	/	Ribose nucleic Acid
mRNA	/	Message RNA
EIS	/	Electrochemical Impedance Spectroscopy

# 1 INTRODUCTION

This section starts with the background of this project followed by the DNA biological concept, and then the proposed novel passive wireless DNA sensor is demonstrated.

## 1.1 Background

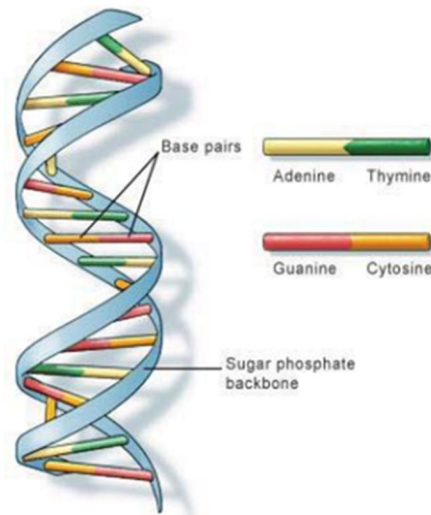
The concept of biosensors, initially introduced by Millan and Mikkelsen [2] in 1993, was discussed and numerous groups have carried out extensive studies in this area. A biosensor is generally defined as a device designed to detect or quantify a biochemical molecule such as a particular DNA sequence or particular protein [3]. Most molecular biosensors are affinity-based, meaning their role is to create an immobilized capture probe that binds the molecule being sensed, thus changing the problem of detecting the analyte in solution to detecting a change at a localized surface where the interaction of the analyte with the bio-receptor is designed to produce an effect measured by the transducer, which might be an electrochemical transducer, optical transducer, gravimetric transducer, Surface Plasmon Resonance (SPR) or electric transducer. An example of a biosensor can be our own body with its own biological recognition system demonstrated with every function of its complex yet efficient human body. This example can be related to the wireless DNA sensor transducer having the ability to detect DNA with different electrochemical detection methods. Using this approach the electrochemical methods the immobilization and hybridization of the DNA can be quantified using specialized equipment that analyzes the data reading the sensitivity of the sensor. Impedance and capacitance analysis are the electrical measurements that indicate the sensitivity of the sensor when it is exposed to the DNA sample.

The most promising applications of electrical biosensors are situations where low cost, small instrument size, and speed of analysis are crucial, but cutting-edge accuracy and detection limits are not. Point-of-care diagnostics—a measurement and diagnosis at a bedside, in an ambulance, or during a clinic visit – are a promising application. If the cost and time per data point were reduced, screening for various disease markers using an electrical biosensor could become part of routine medical checkups [3].

## **1.2 DNA Biological Concept**

DNA, abbreviation of Deoxyribonucleic acid, contains unique genetic information for every living organism present on earth. As shown in Fig. 1, there are two strands of DNA molecules twisting and coupling each other, in the shape of a double helix configuration connected together by four base elements, or nucleotides. These four base elements are, Adenine (A), Cytosine (C), Guanine (G) and Thymine (T). The order in which the base pairs (nucleotides) appear on the helix defines the unique signature of a particular organism or person [4].

A unique condition of DNA bonded pairs is that the pairs Adenine and Thymine will only bond with each other meanwhile Guanine and Cytosine will only bond with each other [4]. This condition enables identifying the DNA sequence, which enables identification of several diseases as well as biological threats, during DNA immobilization and hybridization and also validates the fact that a single strand of DNA molecule could only bind with unique complementary strand with specific DNA sequence when exposed to target.



U.S. National Library of Medicine

**Fig 1.1 Structure of DNA from U.S National Library of Medicine**

### **1.3 The Proposed DNA Sensing System**

This proposed project is focused on detecting DNA through immobilization and hybridization using a novel passive wireless LC circuit and converting the invisible DNA behavior information into a measurable shift---electrical signals. There is an innovative sensing system consisting of an interdigital capacitor and planar inductor, but together with the remote reader, will accomplish DNA immobilization and hybridization monitoring instead of traditional off-the-shelf electronic components. The related electrical change due to DNA molecule behavior is coupled with the resonant frequency acquired by the remote antenna, which carries out the function of remote power supply and wireless communication.

The power delivery and wireless data communication is presented and illustrated in Fig. 1.2. The frequency response of the sensor is remotely detected by monitoring the impedance across the

terminals of the wide bandwidth reader antenna which actually also plays the role as a power transmitter by sending out an oscillating magnetic field via inductive link.

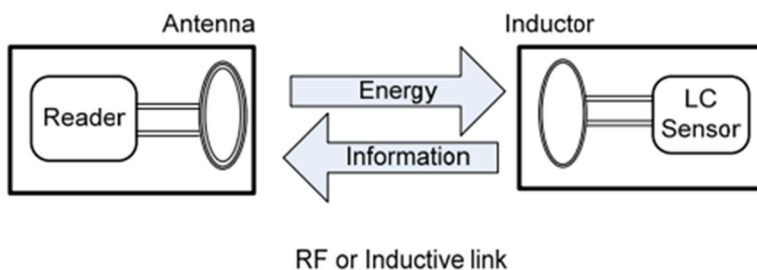


**Fig 1.2 The proposed wireless sensor scheme**

The resonant frequency of the sensor is defined as the peak point where a sudden change appears in the frequency response of the impedance. This resonant frequency is changed when the sensor is exposed to single or double strands of DNA solution. The behavior of DNA attached onto metallic and semi-metallic surfaces has shown potential application in biomedical devices. Because of this, the overall goal of this project is to develop a biosensor that can detect or identify different diseases that are characterized by a specific DNA sequence and provide a stable accurate measurement with a passive wireless and reusable feature, which enables a long-term DNA molecule detection and integrated wireless communication.

## **1.4 Research Objective**

The primary goal of the proposed research is to conduct basic electrochemical research into DNA capacitive sensing mechanism and DNA/surface interfacial conformational characterization

during DNA hybridization process with passive wireless integrated sensor technologies in order to develop an innovative DNA sensing platform for environmental and biomedical applications. The objective of this multidisciplinary research effort is to transform conventional DNA research and RFID technologies into a versatile wireless DNA sensing platform with expected features of label-free, electrochemical characterization, small footprint (lab-on-a-chip), high sensitivity in parts-per-billion, very low cost (a few dollars), passive and wireless integrated, suitable for large scale production, and disposable. Specifically, the proposed research project will:

- 1) develop a passive wireless sensing platform with optimized interdigitated capacitive sensing element for DNA modification and hybridization event monitoring;
- 2) establish an experimental setup and electronics readout system that provide remote power to the DNA sensor and wireless communication means to measure the changes in electrical parameters due to DNA modification and hybridization on the sensing electrodes,
- 3) characterize DNA/surface interfacial conformational changes and study DNA sensing mechanism during DNA modification and hybridization processes with the proposed passive wireless DNA sensing platform;
- 4) design DNA material and self-assembled monolayer (SAM) protocol to immobilize single stranded DNA (ssDNA) probes on gold electrodes and integrate DNA functionalized material into remote sensing platform for biomedical and environmental sensing applications;
- 5) demonstrate a prototype of the proposed wireless DNA detection and hybridization characterization system in laboratory setup.

## **1.5 Thesis Organization**

A review of existing DNA sensing technologies will be discussed in Chapter 2. Modern techniques involved in DNA detection will be compared with sensing principles and various applications. In Chapter 3, DNA sensing mechanism in interdigital electrodes will be assessed. Design considerations of interdigital capacitor will be discussed and simulated by analyzing all the contribution of geometry properties to the change of the capacitance. After that, the DNA sensing principles is demonstrated and the section of the proposed capacitor based on the LC circuit system working performance will be presented in Chapter 4. The experimental setup and sensor characterization will be discussed in Chapter 5 to indicate a promising result. Finally, this work will conclude with a discussion of the thesis contributions and future work on the possibility of the improvements in Chapter 6. The appendix afterwards demonstrates the theory and calculation of a novel configuration of planar inductor other than the conventional one. The sensor fabrication with basic MEMS techniques will be described in the end as references.

## 2 LITERATURE REVIEW

The detection of DNA hybridization has been possible with electro active molecules that monitor the electron transfer mechanism during the hybridization process which present a potential application for the creation of biosensors.

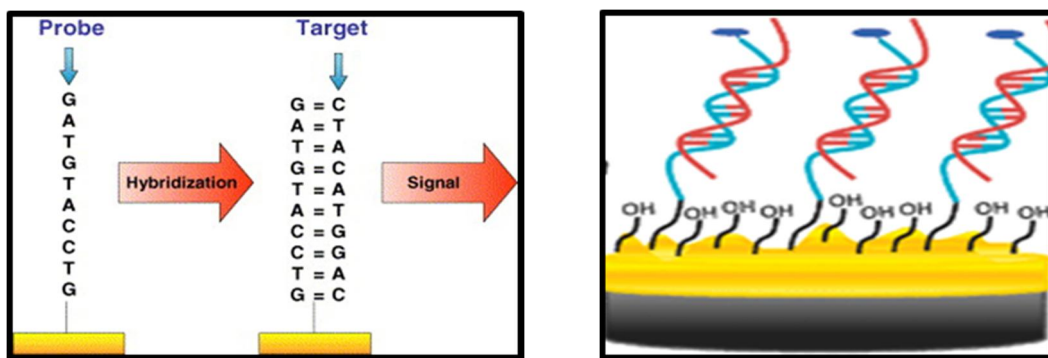


**Fig 2.1** On the left, the steps involved in the detection of a specific DNA sequence using an electrochemical DNA hybridization sensor. On the right, a scheme showing one of the modifications involved in this research, the indirect modification, during the detection of a specific DNA sequence [5].

It has been shown that the sensor performance (e.g., sensitivity, selectivity and stability) is highly dependent on properties of immobilized DNA probes such as orientation, conformation and surface density [5]. Generally, the sensitive element for a DNA biosensor is composed of single stranded DNA (ssDNA) molecules that allow the hybridization of complementary strands [6]. Different methods have been employed to convert these hybridization signals: 1) optical transducers that are based on fiber optics (reflection interference contrast microscopy [7], surface plasmon resonance [8] and Raman spectroscopy [9], 2) electrochemical transduction [10, 11] or electrical transduction (i.e. integrated-circuit biochip [12]) and 3) piezoelectric transduction (measurement of changes in mass) [13].

Of all the above, electrochemistry offers great advantages over the existing devices based on optical schemes, because electrochemical methods provide rapid, simple and low-cost point-of-care- detection of specific nucleic acid sequence [14]. There are several ways to detect DNA by using electrochemistry [15, 16]. Direct methods monitor the oxidation or reduction of DNA, while indirect methods measure the response of redox active molecules or intercalators (antibodies, metal complexes, organic dyes) [17]. Therefore, in the last three decades different types of sensors for biomedical purposes have been developed. As for example, Kelley et al. studied the interaction of methylene blue into the thiol terminated self-assembled monolayer (SAM) of double strand DNA (dsDNA) on gold electrodes by chronoamperometry, cyclic voltammetry, ellipsometry and  $^{32}\text{P}$  labeling methods [18]. Using these as a reference, Ozsoz's et al worked in collaboration with J. Gooding were able to detected the DNA hybridization using methylene blue and self-assembled alkanethiol monolayer on gold electrodes. The purpose of this label-voltammetric determination was to develop a simple novel DNA immobilization strategy, which provides a well-defined recognition interface, onto a SAM of 3-mercaptopropionic acid [19].

Another technique recently used to monitor the extent of DNA immobilization and hybridization due to its sensitivity to the electron transfer is based on DNA microarrays, which were born in response to the completion of a number of whole genome sequences to investigate the resulting large numbers of characterized genes [20]. The power of this technology was demonstrated primarily by the work of Affymetrix [21, 22, 23] and Stanford University groups of DeRisi and Brown. [24, 25, 26] Different studies shows that DNA microarrays have been used to measure mRNA [27] and miRNA [28] expression, to characterize single nucleotide polymorphisms [29] and as a diagnostic tool to determine chromosome amplification. Although

DNA microarrays offer rapid and highly sensitive analytical tools for genetic detection, there are some important challenges that need to be achieved like the integration of microelectronics to microchip-based nucleic acid technologies in a scalable process.

The behavior of DNA attached onto metallic and semi-metallic surfaces has shown potential application in biomedical devices [30]. Because of this, the overall goal of this project is to develop a biosensor that can detect or identify different diseases that are characterized by a specific DNA sequence, such as Anthrax and Tuberculosis. In the case of Anthrax, human infection is due to the bacterium *Bacillus Anthracis* (B. Ant.). This bacterium has the ability to outwit the body's immune system. B. Ant. acquires some extra DNA (plasmid) that can be used as a vector for the introduction of new genes into a bacterial cell allowing B. Ant. to produce deadly toxins and to build a protective shell called a capsule. On the other hand, Tuberculosis is caused by the pathogenic bacterium *M. Tuberculosis* (M. Th.). This is a gram-positive bacterium that requires oxygen to grow and it is primarily a pathogen of the mammalian respiratory system. The infection can be described in three stages [31]. The first one will be is the aerosol transmission of droplets containing M. Th. from an infected individual to a healthy individual. Once within the lungs, M. Th. enters and resides within alveolar macrophages and dendritic cells. The next stage is characterized by the emergence of cell-mediated immunity and the formation of granulomas; and final stage is when latent and controlled M. Th. infection is reactivated [31].

The genome of both bacteria have been studied, showing a 99% similarity of DNA sequence for both bacteria [32, 33]. Therefore, by knowing the DNA sequence, the diseases that these bacteria cause can be detected using a DNA hybridization sensor. Is important to mention that these are not the only type of diseases that can be detected with a DNA hybridization sensor.

Nonetheless, we chose these diseases because the mortality rate is really high (around 75% for anthrax and 45-50% for tuberculosis) and because the methods available for detection are time consuming. It has been reported that B. Ant. spores had been detected in powder samples using Raman Spectroscopy. As for M. Tb., the diagnosis of tuberculosis involves skin tests, chest X-rays, sputum analysis, and PCR tests to detect the genetic material of the causative bacteria [34]. All of these are time-consuming, expensive and equipment requirement producers. For this reason, an easy, non-expensive and fast detection technique is required.

It had been proved that no fluorophores or secondary transducers are necessary to sense DNA target for hairpins or single strand DNA [30], if EIS is employed. Therefore, we can classify this process as a label-free DNA detection, which involves the measurement of physiochemical changes occurring on the surface of the transducer device due to the DNA hybridization [20] Based on this, we proposed to develop a capacitive free label lab-on-chip technology using passive Wireless technology that will allows us to detect the disease in a more accurate and faster manner. The sensing element will include DNA modified electrodes with capacitive sensitivity in the ppb range by differential capacitance changes from DNA functional surfaces.

## 3 INTERDIGITAL CAPACITANCE

This chapter starts with a brief introduction of typical interdigital electrode and capacitance computation of the interdigital array electrode capacitor with multi-layered structure and an input function is being developed in Mathematica 8.0©software. After the exploration of the geometry dependent capacitance of the interdigital capacitor, the design consideration of proposed sensor will be indicated. Meanwhile, validation and simulation can be carried out to discuss how to determine optimized structure of electrodes.

### 3.1 Introduction

Interdigital capacitors (IDC) for technological applications have been studied by many authors since the early 1970s. A lot of applications using this structure include their uses in lumped elements for microwave integrated circuits [35, 36], optical and surface acoustic wave devices [37], optically controlled microwave devices [38], thin-film acoustic–electronic transducers and tunable devices [39], dielectric studies on thin films [40] and chemical sensors [41]. Before we prepare for discussing the principle of interdigital capacitive sensors (IDC-S), an approximation model is briefly illustrated in Fig. 3.1.

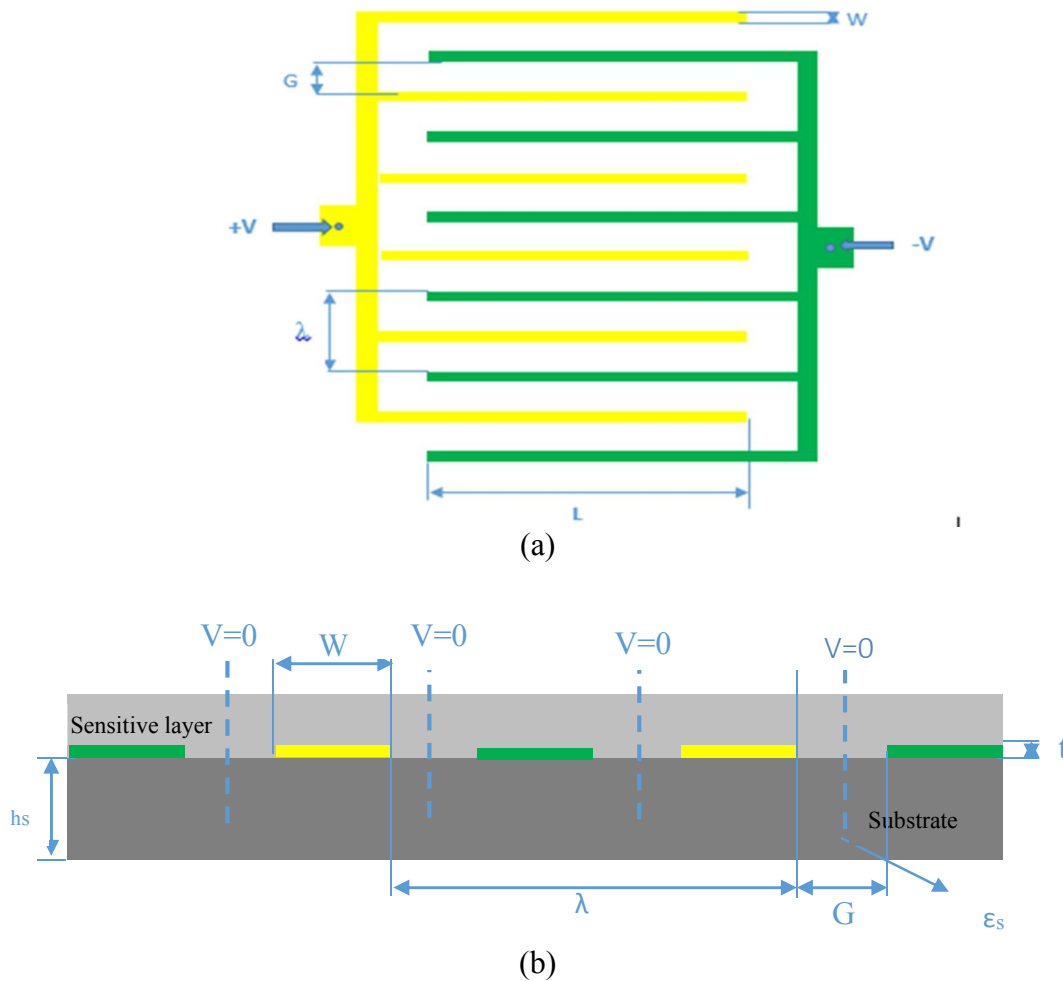


**Fig 3.1 (a) Layout of electrode plane; (b) Cross-section of a periodic IDC-S.**

Fig. 3.1 Shows that a layout of IDC, of which the induction electrode is in the same plane as driving electrode and consists of two interpenetrating comb electrodes. The gaps between electrodes have a width  $G$  while the fingers have a width  $W$ . The thickness of electrodes is height  $t$  and the thickness of the substrate is marked as  $h_s$ . The permittivity constant of the substrate is  $\epsilon_s$ . Each electrode is connected with opposite potential (either  $+V$  or  $-V$ ). Thus two dimensionless parameters are revealed:

- The ratio between the space and finger widths ( $\eta = W/W+G = 2W/2(W+G) = 2W/\lambda$ );

- The ratio between the thickness of the sensitive layer and the spatial sensor wavelength ( $r=h/\lambda$ ).

These two parameters are strongly dependent on the value of capacitance, as will be shown in the next sections.

By symmetry due to system geometry, the whole system can be divided into a number of identical unit cells with dimension  $\lambda/2$ , from the center of electrode to the mid-point of adjacent pole. Therefore this assembly simplified our research procedure in respect to expression and calculation.

In a geometrically symmetrical capacitor, the perpendicular planes halfway between electrodes are equipotential planes. In common practice, this plane is considered as an electric ground and its voltage is set to zero. The electric field lines cross normal to this plane as shown in Fig. 3.2.

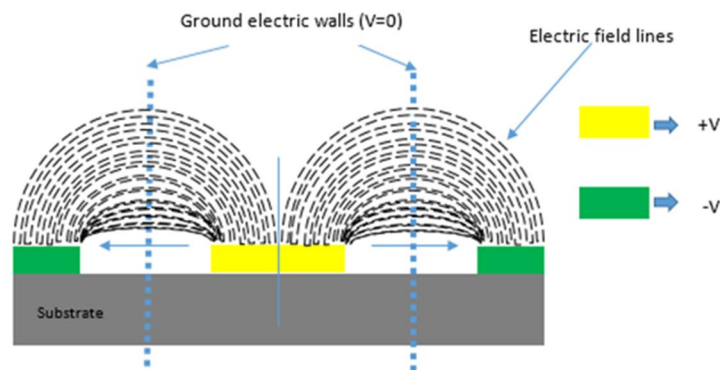


**Fig 3.2 Unit cell model of the proposed multi-layered interdigital capacitor**

By effectively and reasonably ignoring the parasitic influence on the IDEs finger edges and ends, the analysis of the IDC is simplified. Furthermore, more remarkable, during experiment we can neglect some unnecessary factors: Polarization phenomena, the thickness of the electrodes (much thinner than width), of course, since they are much greater than the wavelength, the length

of electrodes strip can be considered infinite. Therefore, under this assumption, the entire IDC is predigested into a single unit cell as a straightforward model mentioned above. However, this is still a 3-D problem for electrical field.

## **3.2 Theory and Calculations**

Earlier development efforts on finding the complex impedance between interdigital electrodes were dedicated [57, 58]. However, this task is not a trivial one. Even 2-D approximation of the interdigital structures results in the electric field distribution that is too complex to be described rigorously by simple algebraic expressions. The potential distribution along the sensor-material interface between the two ports is not known in advance, and depends on the material properties and geometric parameters of the structure.

Mathematical description for a so-called continuum model was developed in the 1980s and 1990s. The representation of electric potential with spatial Fourier modes falls between closed-form analytical solutions and numerical techniques to solve the conservation of charge boundary condition between electrodes. It is less difficult than traditional numerical approaches, but it does not offer analytical expressions suitable for extensive manipulation. Being limited to multiple-layer problems, the continuum model does not possess the generality of numerical techniques that allow computation of electric fields associated with arbitrary shapes [42].

Electromagnetic (EM) simulators based on finite element method (FEM) has been used extensively for calculation of transmission coefficient, impedance and capacitance matrices. Frequently used electromagnetic simulators include Agilent Momentum for unshielded numerical integration based planar analyses (Agilent® Technologies), Ansoft HFSS for 3 dimensional

arbitrary frequency domain analyses (Ansoft® Corporation), CST Microwave Studio for 3 dimensional arbitrary time domain/wideband frequency domain analyses (Computer Simulation Technology) and Sonnet for shielded FFT based planar analyses (Sonnet®).

Another potentially useful approach for the calculation of 2D interdigital electrode capacitance stems from conformal mapping. Conformal mapping is one of the most frequently used approaches to transform an appropriate space region of IDC to a parallel plate capacitor geometry whose capacitance value can be calculated. Typical examples of such analysis and analytical solutions for IDC capacitance are given by Endres et al in 1991 [43] and Igreja [44], as the calculation method in the following section.

### 3.2.1 Single semi-infinite layer capacitance

We first calculate the capacitance of a semi-infinite layer above the electrode plane using an equivalent electric circuit [44].

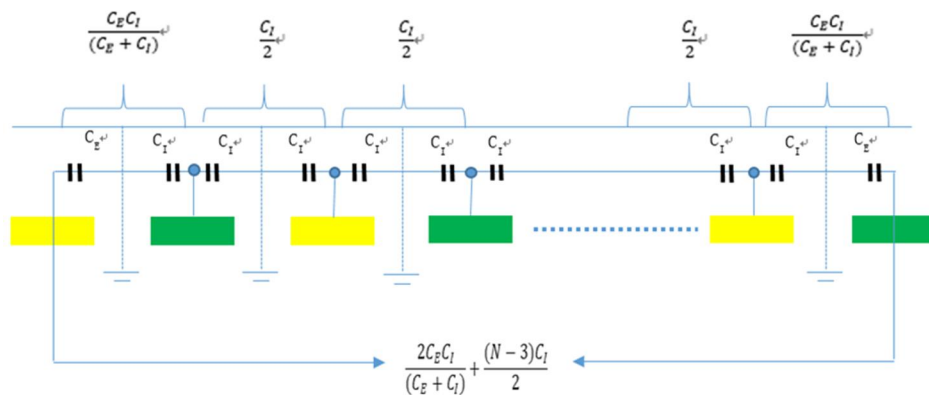


**Fig 3.3 Schematic of the equivalent circuit for evaluation of the static capacitance of a semi-infinite top layer in a periodic IDC-S with N electrodes.**

Close inspecting Fig. 3.3, it is not hard to unveil that the total capacitance between positive and negative electrodes of a semi-infinite layer IDC-S is presented as below:

$$C = (N-3) \cdot C_I / 2 + 2C_I \cdot C_E / (C_I + C_E), N > 3 \quad (3.1)$$

Where,

N ----- The number of electrodes.

$C_I$  ----- The capacitance of one interior electrode relative to the ground potential.

$C_E$  ----- The capacitance of one outer electrode relative to the ground plane next to it.

The capacitance with the two or three layers structures cannot be included in the scope of this work, however these structures can be easily developed with small modifications of the present model [44]. On the other hand, we can figure out as the number of electrodes increases,  $C_E \approx C_I$ , so that we can derive equation 3.1 into  $C \approx (N - 1) / 2 \cdot C_I$ . For many practical cases, we only need to calculate  $C_I$ .

### 3.2.2 *N-layer capacitance*

As discussed in previous section, the total capacitance of multi-layer capacitor can be determined by two different geometrical variables:  $C_I$  and  $C_E$ , which can also be calculated for a sensor having one or more finite dielectric layers (of different permittivity and thickness) on the top of the electrodes using the so-called partial capacitance technique [44].

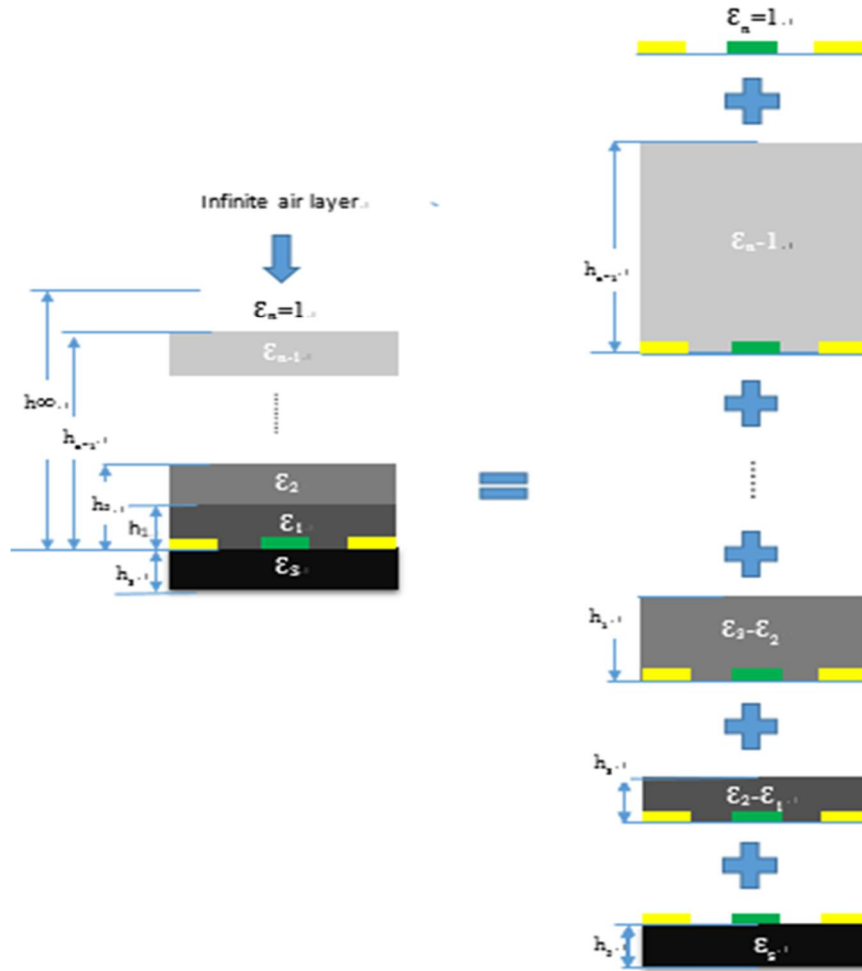


**Fig 3.4 Splitting of a N-layered plane according to the partial capacitance technique.**

The picture shows us the schematic (upper layer with N layers and infinite air and s thick substrate layer) to explain how to deal with the calculation of capacitance of multi-layered structure electrodes. We can obtain (In most case,  $\epsilon_n$  equals to 1 since infinite air on the top):

$$C_I = \sum_{i=1}^{n-1} (\epsilon_i - \epsilon_{i+1}) * C_I (h_i) + (\epsilon_n + \epsilon_S) * C_I(\infty) \quad (3.2)$$

$$C_E = \sum_{i=1}^{n-1} (\epsilon_i - \epsilon_{i+1}) * C_E (h_i) + (\epsilon_n + \epsilon_S) * C_E(\infty) \quad (3.3)$$

Where,

$C_I$  ----- the interior capacitance of multi-layer plane.

$C_E$  ----- the exterior capacitance of multi-layer plane.

$\epsilon_i$  ----- the relative permittivity of the  $i^{\text{th}}$  layer.

$\epsilon_s$  ----- the permittivity of the inert substrate.

$C_I(h_i)$  ---- the geometric capacitance of  $i^{\text{th}}$  layer with height  $h_i$  for inner fingers.

$C_E(h_i)$  ---- the geometric capacitance of  $i^{\text{th}}$  layer with height  $h_i$  for outer fingers.

As usual the substrate thickness is much greater than  $\lambda$ , so we can assume that inert substrate is playing a role as most outer layer in lower plane instead of infinite air, as a result of geometric dependent sensitivity of capacitance that we will demonstrate in latter section. However, more remarkable, if thickness of substrate is close to  $\lambda$ , we cannot ignore infinite air below thin substrate, but calculate it in the same way as partial capacitance technique for upper layer.

### 3.2.3 Computation of $C_I(h_i)$ and $C_E(h_i)$

In last section, we have known the total upper capacitance of the sensor can be calculated as previously described inserting Eq. (3.2) and Eq. (3.3) to Eq. (3.1). We will use conformal mapping techniques to map an appropriate space region of the IDC-S onto a parallel plate capacitor geometry for which the capacitance value is known as well as the equipotential lines and the lines of the electric field. As the conformal transformation is analytic, it can be shown that the capacitance in the original space region will transform accordingly [44].

The capacitances of the IDC unit cell with infinite layer and finite layer at interior or exterior electrodes are described using a complete elliptic integral of the first kind  $K[k]$ . The detail calculations are shown in Table 3.1.

**Table 3.1 Detailed equations needed for the calculation of  $C_E$  and  $C_I$  for PPC case [44]**

	Interior electrodes	Exterior electrodes
Finite layer	$C_I = \epsilon_0 \epsilon_r \frac{K(k_I)}{K(k'_I)}$ $k'_I = \sqrt{1 - k_I^2}$ $k_I = t_2 \sqrt{\frac{t_4^2 - 1}{t_4^2 - t_2^2}}$ $t_2 = \text{sn}(K(k)\eta, k)$ $t_4 = \frac{1}{k}$ $k = \left( \frac{v_2(0, q)}{v_3(0, q)} \right)^2$ $q = \exp(-4\pi r)$	$C_E = \epsilon_0 \epsilon_r \frac{K(k_E)}{K(k'_E)}$ $k'_E = \sqrt{1 - k_E^2}$ $k_E = \frac{1}{t_3} \sqrt{\frac{t_4^2 - t_3^2}{t_4^2 - 1}}$ $t_2 = \cosh\left(\frac{\pi(1 - \eta)}{8r}\right)$ $t_4 = \cosh\left(\frac{\pi(1 + \eta)}{8r}\right)$
Infinite layer	$C_I = \epsilon_0 \epsilon_r \frac{K(k_{I\infty})}{K(k'_{I\infty})}$ $k_{I\infty} = \sin\left(\frac{\pi}{2}\eta\right)$	$C_E = \epsilon_0 \epsilon_r \frac{K(k_{E\infty})}{K(k'_{E\infty})}$ $k_{E\infty} = \frac{2\sqrt{\eta}}{1 + \eta}$

where  $K(k_I)$  is the complete elliptic integral of the first kind with modulus  $k$ ,  $k'$  is the complementary modulus of  $k$ ,  $v_2$  and  $v_3$  are the Elliptic theta functions,  $\text{sn}(z, k)$  is the Jacobi elliptic function of modulus  $k$ ,  $\lambda=2(G+W)$  is the spatial wavelength,  $\eta$  is the ratio between the electrode width and the unit cell width which is known as the metal ratio, and  $r$  is the ratio between the thickness of each layer and the spatial wavelength.

From Eq. (3.1) and Table 3.1, we can demonstrate that the capacitance for a particular sensor configuration is a function of the dielectric permittivity of the materials, the fingers length, the

number of electrodes comb and of two geometric non-dimensional parameters below:  $r$  and  $\eta$ . In other words,

$$C=C(\eta, r, \epsilon_i, N, L, \epsilon_s). \quad (3.4)$$

Where,

$\eta$  ----- The Metal ratio.

$r$  ----- The geometric parameter defined as  $r=h_i/\lambda$ .  $h_i$  is the thickness of each layer.

$N$  ----- The number of interdigital electrodes.

$L$  ----- The length of each electrode.

$\epsilon_i$  ----- The permittivity of  $i^{\text{th}}$  layer.

$\epsilon_s$  ----- The permittivity of the substrate.

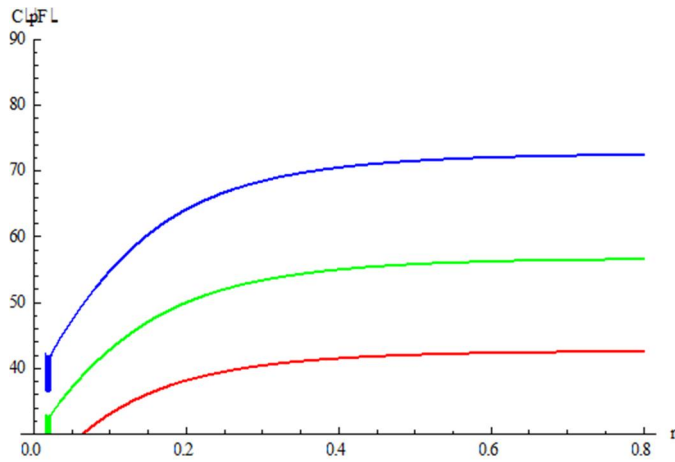
### 3.3 Result and Discussion

As noticed in Eq. (3.5), the impact of geometry on the capacitance of IDC cell manifests on the parameter such as  $N$ ,  $L$ ,  $\eta$ ,  $r$ . Therefore the dependence of capacitance on these four parameters has been studied. In this study, the discussed ranges of parameters  $\eta$  and  $r$  is from 0.1 to 0.9 and from 0.1 to 0.8, respectively. Other parameters are set as follows:  $\epsilon_s=3.15$  and  $N=100$ ,  $L=20\text{mm}$ .

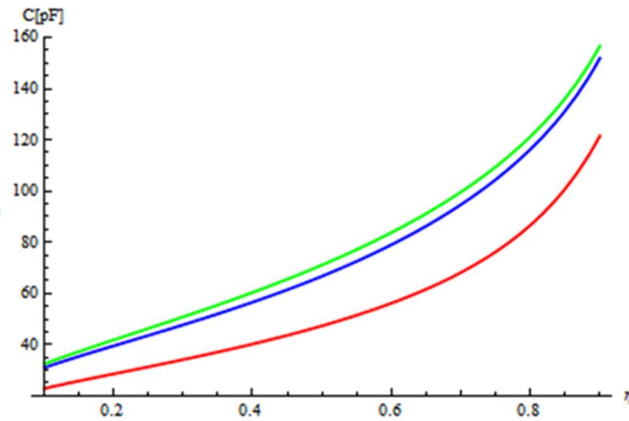
The calculated capacitance of an IDC at a fixed metal ratio with respect to  $r$  is shown in Fig. 3.5(a). In the range from 0 to 0.5 of  $r$ , the increasing substrate thickness leads to the increase of the capacitance and the capacitance reaches a maximum value at  $r=0.5$ . Then there is not significant increase anymore with further increasing the value of  $r$ . In a word, the capacitance of IDC increases smoothly and logarithmically with the increasing value of  $r$ .

Related calculated capacitances with respect to each selected  $\eta$  are plotted in Fig. 3.5(b). The capacitance of IDC increases smoothly with the increasing value of  $\eta$ , especially increasing exponentially when the value of metal ratio  $\eta$  is close to 0.8. In the case of metal ratio  $\eta=0.2$ , the

unit cell has a wide gap and narrow finger. On the other hand, in the case of metal ratio  $\eta=0.8$ , the unit cell has a narrow gap and wide finger. As can be seen in the Fig. 3.5(b), the same amount of variation in metal ratio results a more significant change when the initial metal ratio is bigger than 0.9, which means that the interdigital capacitor with a higher metal ratio shows greater sensitivity than the one with a smaller metal ratio. Therefore, in our design of the interdigital capacitor, we tend to set the metal ratio at 0.9.



(i) Red line for  $\eta=0.2$ , (ii) Green line for  $\eta=0.35$ , (iii) Blue line for  $\eta=0.5$



(i) Red line for  $r=0.05$ , (ii) Blue line for  $r=0.25$ , (iii) Green line for  $r=0.45$

**Fig 3.5 Capacitance as a function of  $\eta$  and  $r$**

Based on above analysis and close inspection of the Fig. 3.5 (a) and (b), it suggests that a bigger metal ratio and a bigger value of  $r$  provide a higher capacitance. Therefore, for the practical purpose it is desirable that the IDC incorporate a small unit cell (since  $r=h/\lambda$ , experimental  $h$  is constant) with a big metal ratio. Moreover, to get a stable capacitance that is not influenced by the substrate, the thickness of the substrate must be bigger than 40% of the unit cell length (so that we can treat substrate as infinite layer). However, as noticed in the range 0.8-0.9 of  $\eta$  the change of capacitance is nonlinear and hard to handle, although it gets much more sensitive in this range. Consequently, in order to have a better sensing linearity, in real design, we are trying to avoid this range and get a compromising range such as 0.6-0.7.

## **3.4 Further Discussion**

### *3.4.1 Brief Introduction*

In a previous section, as shown in Eq. (3.3) and Eq. (3.4), we proposed a model for the computation of the capacitance of these multi-layered structures using the techniques of conformal mapping and partial capacitance, until now, which has been used in applications where the permittivity of consecutive layers monotonically decreases from layer to layer (as we move away from the electrodes plane) giving excellent results. New applications, such as the use of Si/SiO<sub>2</sub> substrates (to promote very smooth surfaces for electrodes deposition) or the use of passivation

layers for the protection of electrodes (e.g. from liquids), among others, represent a new challenge for the computation of the overall capacitance since in these devices the permittivity cannot decrease from layer to layer [46]. In other words, the partial capacitance (PC) technology and conformal mapping (CM) technology we used to calculate capacitance of planar interdigital electrodes in multi-layered structures where the permittivity decreases monotonically from layer to layer had given very accurate results. However, as we mentioned, the original PC is not suitable to be used in multi-layered structures in which the permittivity increases monotonically as we move away from the electrodes. In this later case, we are supposed to modify the original PC technology to include these new configurations. In this section we will discuss a new approach, splitting the concept of partial capacitance in parallel partial capacitance (PPC) and serial partial capacitance (SPC) where new conformal mapping transformations are proposed for the latter case [46].

### *3.4.2 Theory and Calculations*

With respect to computation of multi-layered structure electrodes capacitance, we can use the same equation as before (see Eq. (3.1)) and we only have to model one half-plane because of the same way to obtain another one. It is remarkable that for each half-plane we will divide the problem into two different possibilities (as proposed by Ghione [47]). (i) There is a monotonic decrease in the permittivity from layer to layer as we move away from the electrodes plane; (ii) There is a monotonic increase in the permittivity from layer to layer as we move away from the electrodes

plane. For the mixed case, in general, the way cannot provide a satisfactory approximation. We just talk about the first two cases.

For case (i), we have discussed in the previous section, as shown in Eq. (3.3) and Eq. (3.4), and is summarized in the Table 3.1.

For case (ii), as we mentioned before, the total capacitance of upper-part of electrodes can be evaluated with geometric capacitance  $C_{I,U}$  and  $C_{E,U}$  using Eq. (3.1).

$$C = (N-3) * C_I / 2 + 2C_I * C_E / (C_I + C_E), N > 3 \quad (3.1)$$

In addition,  $C_{I,U}$  and  $C_{E,U}$  are decided by contribution of sum of individual layer, which in turn, each one, can be studied by the method of Conformal Mapping. The total contribution from all  $n$  layers should be now computed as [46]:

$$1/C_I = \sum_{i=1}^{n-1} (1/\epsilon_i - 1/\epsilon_{i+1}) * 1/C_{IP}(H_i) + 1/\epsilon_n * 1/C_I(\infty) \quad (3.6)$$

$$1/C_E = \sum_{i=1}^{n-1} (1/\epsilon_i - 1/\epsilon_{i+1}) * 1/C_{EP}(H_i) + 1/\epsilon_n * 1/C_E(\infty) \quad (3.7)$$

Where  $\epsilon_i$  is the relative permittivity of the  $i^{\text{th}}$  layer,  $C_{IP}(H_i)$ ,  $C_{EP}(H_i)$  are the geometric capacitance of layer  $i$  between layer  $i$  and layer  $i+1$ , for the inner and outer fingers, respectively,  $H_i$  is the layer height (measured from the plane of the electrodes),  $C_I(\infty)$  and  $C_E(\infty)$  are the geometric capacities for a layer with infinite height (utmost outer layer). Hence, similar to Table 3.1, the capacitance of each layer, where the permittivity increases monotonically layer by layer, can be evaluated by Table 3.2.

**Table 3.2 Detailed equations for the calculation of  $C_E$  and  $C_I$  for SPC case [44]**

	Interior electrodes	Exterior electrodes
Finite layer	$C_I = \epsilon_0 \epsilon_r K(k_I) / K(k_I')$	$C_E = \epsilon_0 \epsilon_r K(k_E) / K(k_E')$
	$k_I' = \sqrt{1 - k_I^2}$	$k_E' = \sqrt{1 - k_E^2}$
	$k_I = t_2$	$k_E = \sqrt{\frac{t_4 - t_3}{t_4 - 1}}$
	$t_2 = \text{sn}(K(k)\eta, k)$	$t_3 = \cosh\left(\frac{\pi(1-\eta)}{4r}\right)$
	$t_4 = 1/k$	$t_4 = \cosh\left(\frac{\pi(1+\eta)}{4r}\right)$
	$k = \left(\frac{v_2(0, q)}{v_3(0, q)}\right)^{1/2}$	
	$q = \exp(-4\pi r)$	
Infinite layer	$C_I = \epsilon_0 \epsilon_r K(k_{I\infty}) / K(k_{I\infty}')$	$C_E = \epsilon_0 \epsilon_r K(k_{E\infty}) / K(k_{E\infty}')$
	$k_{I\infty} = \sin\left(\frac{\pi}{2} * \eta\right)$	$k_{E\infty} = 2\sqrt{\eta} / (1 + \eta)$

where  $K(k_I)$  is the complete elliptic integral of the first kind with modulus  $k$ ,  $k'$  is the complementary modulus of  $k$ ,  $v_2$  and  $v_3$  are the Elliptic theta functions,  $\text{sn}(z, k)$  is the Jacobi elliptic function of modulus  $k$ ,  $\lambda = 2(G + W)$  is the spatial wavelength,  $\eta$  is the ratio between the electrode width and the unit cell width which is known as the metal ratio, and  $r$  is the ratio between the thickness of each layer and the spatial wavelength.

## 4 SELECTION OF SENSOR DESIGN

After discussing the geometry dependent capacitance of the interdigital capacitor, the capacitive effect DNA molecule behavior makes is explored throughout immobilization and hybridization process. In order to get a sensor with best sensitivity, smallest size, longest detection distance and highest quality factor, the design consideration and selection for the sensor together with the interdigital capacitor and the planar inductor are dedicated in this section.

### 4.1 DNA Sensing Principles.

Electrochemical biosensors combine the analytical power of electrochemical techniques with the specificity of biological recognition processes. The aim is to biologically produce an electrical signal that relates to the presence of an analyte. For this purpose, a biospecific reagent is either immobilized or retained at a suitable electrode, which converts the biological recognition event into a quantitative amperometric or potentiometric response.

The success of the most of the electrochemical sensor, especially the ones related with the detection of biomolecules, depends on the immobilization of the analyte on the surface. The objective is to provide an intimate contact between the analyte and the sensing surface while maintaining the stability of the biomolecule under study, in the case the single strand of DNA (ssDNA). There are several physical and chemical schemes that can be used to immobilize the different analytes (Fig. 4.1) [53]. However, for this research we are going to use surface adsorption to immobilize are ssDNA. This method relies on non-specific physical interaction between the biomolecule and the surface of the matrix, brought about by mixing a concentrated solution of

biomolecules with the solid [54]. A major advantage of adsorption is that usually no reagents and only a minimum of activation steps are required.

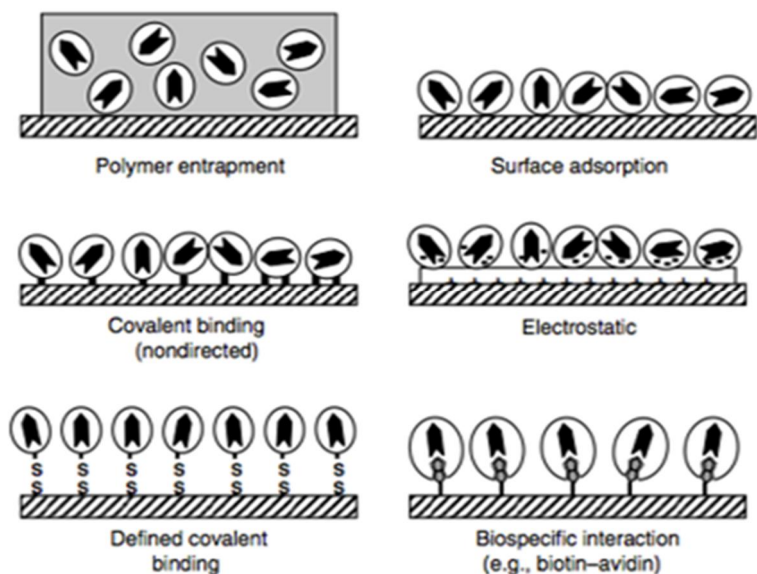


**Fig 4.1 Methods for immobilizing different biomolecules onto electrode surfaces [53]**

Because of the weak bonds involved, desorption of the protein resulting from changes in temperature, pH, ionic strength or even the mere presence of substrate, is often observed, which can be either an advantage or disadvantage [54]. The most significant disadvantage of this type of immobilization method is non-specific, further adsorption of other proteins or other substances as the immobilized enzyme is used, which probably decrease depending on the surface mobility of enzyme and substrate. Nevertheless, in our research the gold surface was functionalized with carboxyl thiol and, by exploiting its -COOH group, 3'-NH<sub>2</sub> modified DNA will be conveniently attached. By doing this, the non-specific adsorptions are removed as the measurement is conducted.

When the gold electrode is clean, the equivalent capacitance is going to be relative small. Once we modified this one with a single strand, the equivalent capacitance will increase. When the hybridization process occurs, the equivalent capacitance obtain is even higher (Fig. 4.2). This behavior is observe because there are more electron energy accumulate to the phosphate groups of the DNA.

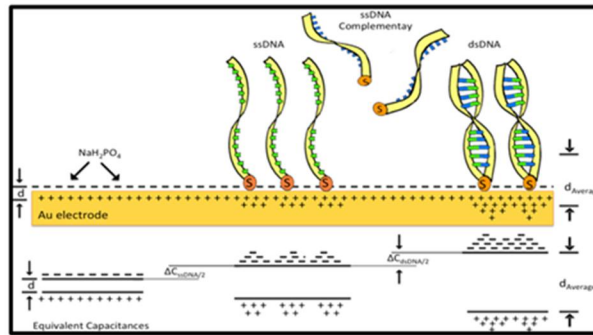


**Fig 4.2 Tendency of the equivalent capacitances for DNA immobilization and hybridization [54]**

## 4.2 Selection of Capacitor Design.

As demonstrated in past chapter, we can deduce the capacitance for a particular sensor configuration is a function of the dielectric permittivity of the materials, the fingers length, the number of electrodes comb and of two geometric dimensionless parameters above:  $r$  and  $\eta$ , In other words,

$$C = C(\eta, r, \epsilon_i, n, L, \epsilon_s) \quad (4.1)$$

Where,

$\eta$  ----- The Metal ratio.

$r$  ----- The geometric parameter defined as  $r=h_i/\lambda$ .  $h_i$  is the thickness of each layer.

$N$  ----- The number of interdigital electrodes.

$L$  ----- The length of each electrode.

$\epsilon_i$  ----- The permittivity of  $i^{\text{th}}$  layer.

$\epsilon_s$  ----- The permittivity of the substrate.

To figure out effect each relevant factor makes on the value and sensitivity of capacitance discussed above, we can assume that there are three capacitor specimen, which can be applied to further analysis through intercomparison, with diverse sets of parameters following:

- 1)  $W1=10\mu\text{m}$ ,  $G1=5\mu\text{m}$ ,  $L=2\text{mm}$ ,  $N=130$ ;
- 2)  $W2=10\mu\text{m}$ ,  $G2=10\mu\text{m}$ ,  $L=2\text{mm}$ ,  $N=130$ ;
- 3)  $W3=5\mu\text{m}$ ,  $G3=5\mu\text{m}$ ,  $L=2\text{mm}$ ,  $N=130$ .

This present paper puts forward a general method to analyze factors with respect to certain objective function and discusses three models mentioned in different configuration.

#### *4.2.1 IDC-S with top air layer*

Despite the fact that a typical IDC-S has usually one layer on the top of the electrodes, it is of scientific interest to compare the results obtained with this model to the available models for an IDC with an infinite top air layer, since this configuration is the most studied one as reference. In this case, there is no sensitive layer above and  $\epsilon_i$  is supposed to be 1 because of bare electrodes

exposed to fresh air, moreover the metallization ration  $\eta$  is fixed and correspond to three sets of geometric parameters, which should be 0.6667, 0.5, 0.5, respectively, obtained by equation below.

$$\eta = \frac{W}{W+G} \quad (4.2)$$

Therefore, the thickness of substrate  $h_s$  concerned with  $r_s$  by  $r_s = h_s/\lambda$  is only factor making sense to capacitance with a same substrate material. Related calculated capacitances with respect to  $h_s$  are plotted and compared with three different available models mentioned above in Fig. 4.3 as we assume permittivity of substrate yields  $\epsilon_s=3.15$ .

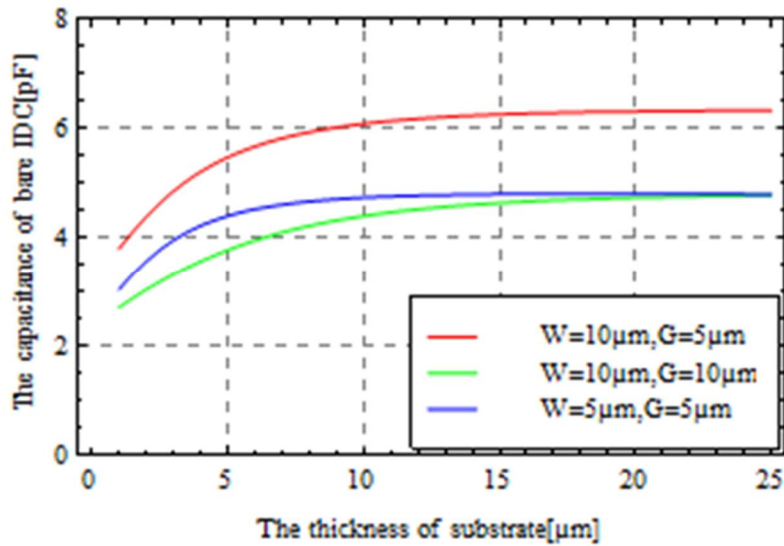


**Fig 4.3 Dependence of capacitance on  $h_s$  with top air layer**

Obviously, the capacitance of IDC increases smoothly and logarithmically with the increasing value of  $h_s$ . In the range from 1 to 25 of  $h_s$ , the increasing substrate thickness leads to the increase of the capacitance until it reaches a maximum value when  $h_s$  equals to 15μm, 20μm, 10μm,

respectively for these models. Then there is not significant increase anymore with further increasing the value of  $h_s$ .

On another side, we can realize model② has a same saturated value as model③, which takes an identical metal ratio  $\eta$ , since there is no more effect on capacitance by  $h_s$ . Therefore, it is indispensable to do an assessment of role of  $\eta$ . In Fig. 4.4, the dependence of the capacitance on the metallization ratio  $\eta$  for a sensor with infinite air layer above the electrodes is shown. The simulation parameters are as follows:  $\epsilon_s=3.15$ ;  $L=2\text{mm}$ ;  $N=130$ .

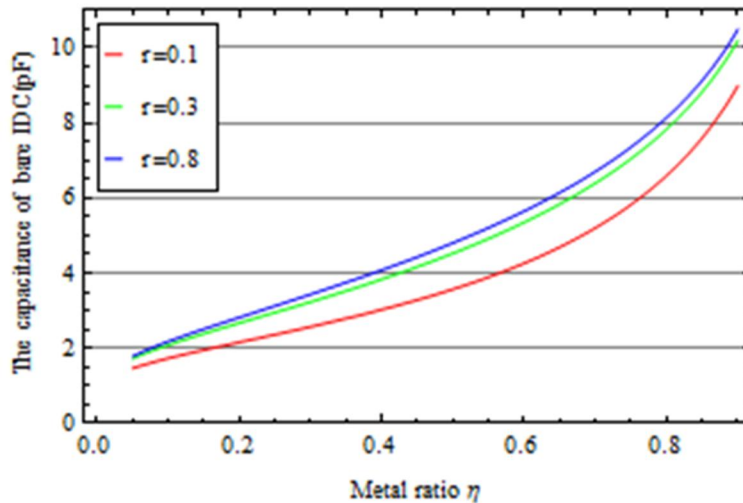


**Fig 4.4 Dependence of capacitance on  $\eta$  with different  $r$**

In Fig. 4.4, the dependence of the capacitance on the metallization ratio  $\eta$  for a sensor with infinite air layer above the electrodes is shown. The simulation parameters are as follows:  $\epsilon_s=3.15$ ;  $L=2\text{mm}$ ;  $N=130$ . The capacitance of bare IDC increases smoothly with the increasing value of  $\eta$ , especially increasing exponentially when the value of metal ratio  $\eta$  is close to 0.9. The unit cell with a higher metal ratio  $\eta$  has a wide gap and narrow finger, vice versa. Close inspecting figure

above, we can verify that the same amount of variation in metal ratio results a more significant change when the initial metal ratio is bigger than 0.9, which means that the interdigital capacitor with a higher metal ratio shows greater sensitivity than the one with a smaller metal ratio. Therefore, in our design of the interdigital capacitor, we tend to set the metal ratio at 0.9.

Based on above analysis of Fig. 4.3 and Fig. 4.4, it suggests that a capacitor with bigger metal ratio and larger value of  $r$  provide a higher capacitance. Therefore, for the practical purpose it is desirable that the IDC is composed of a large number of smaller unit cells with a big metal ratio. Moreover, to get a stable capacitance that is not influenced by the substrate, the thickness of the substrate must be bigger than 50% of the unit cell length as  $h_s = r_{\text{saturated}} * \lambda$  (so that we can treat substrate as infinite layer). However, as noticed in the range 0.8-0.9 of  $\eta$  the change of capacitance is nonlinear. Thus, in order to have a better sensing linearity, in real design, we are trying to avoid this range.

#### *4.2.2 IDC-S with one sensitive layer*

This configuration is of much interest for practical sensing which has a sensitive layer placed on the electrodes since we can track real-time variation of DNA molecules through observing change of capacitance displayed in the reader while process of immobilization and hybridization. Notice that capacitance will respond to a change in the permittivity of sensitive layer and be aroused by the change of height of sensitive layer because of swelling involved.

In Fig. 4.5, the dependence of the capacitance on the height of sensitive layer, which brings about a geometric parameter  $r$  (the ratio between the height of the sensitive layer and the sensor spatial wavelength), for a sensor with one finite layer above electrodes is represented with different

available models mentioned. The simulation parameters are as follows:  $\epsilon_r=5$ ;  $\epsilon_s=3.15$ ;  $\eta_1=0.6667$ ;  $\eta_2=0.5$ ;  $\eta_3=0.5$ ;  $N=130$ ;  $L=2\text{mm}$ .

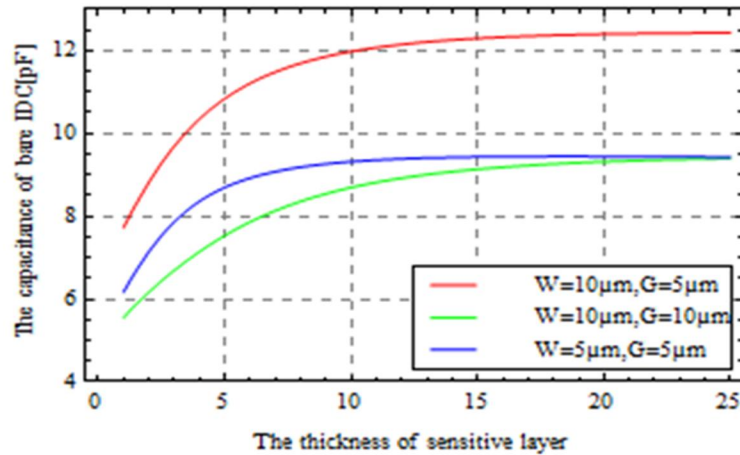


**Fig 4.5 Dependence of capacitance on h<sub>s</sub> with one sensitive layer**

From the figure presented above, it is obvious to show the positive correlation between capacitance and the height of sensitive layer  $h_s$  for all models with diverse geometric parameters. As shown in Fig. 4.6, which is simulated with same parameters as Fig. 4.5, the bigger dimensionless parameter  $r$  we design, the larger capacitance value is obtained, however, the lower sensitivity. Although model② has a similar behavior as model③ since they have an identical metal ratio  $\eta$  and geometric parameter  $r$  at the same time, the height of sensitive layer available to be observed during experiment is different. For model②, if  $r$  is larger than its saturated value, which is equal to 0.5 as shown in Fig, 4.6, the total capacitance of IDC with one sensitive layer will be steady, in other word, if the height of sensitive layer  $h_s \geq r_{\text{saturated}} * \lambda$ , no matter what great change it has on the electrodes, we only get a constant capacitance. Compared to model②, model③ with a shorter wavelength should have a hypersensitivity in detectable range of  $r$  since it has a lower parameter  $r$  under the same height of sensitive layer ( $r=h_s/\lambda$ ). On the other hand, for model① with

higher metal ratio, although taking more space, is easier to be applied to observe the change of capacitance.

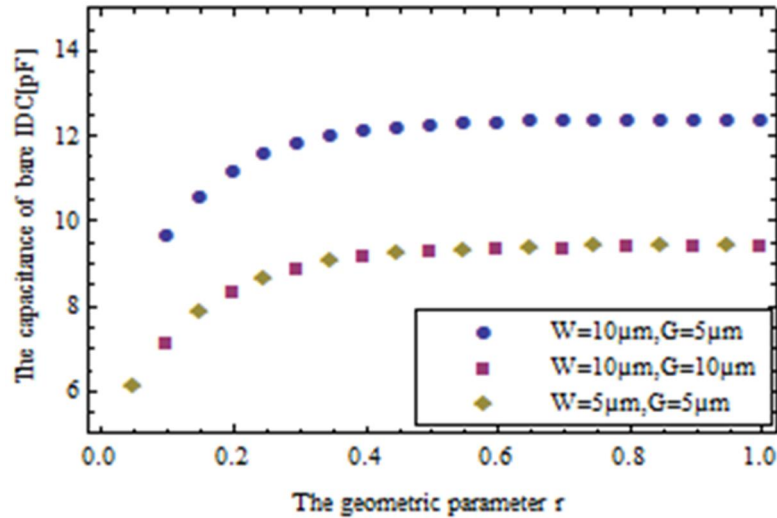


**Fig 4.6 Dependence of capacitance on geometric parameter r**

Other aspect should be taken into consider is change of permittivity of sensitive layer due to hybridization procedure of DNA. Close inspecting Fig. 4.7, with respect to same sensitive layer with identical thickness assumed to be 10μm, we can calculate out the geometric parameter corresponding to these three models mentioned above is 0.33, 0.25 and 0.5 respectively. The rest simulate coefficients following is presented as:  $N=130$ ,  $L=2\text{mm}$ ,  $\epsilon_s=3.15$ . Apparently the change of total capacitance represents an increasing linear behavior with increasing of permittivity of analyte. Compared to Fig. 4.4 and Fig. 4.5, it is easy to demonstrate that the change of permittivity of sensitive takes much more significant effect to capacitance than the change of height of sensitive layer. Consequently, with respect to sensitivity caused by change of permittivity of analyte, model③ and model① are more sensitive for the change of capacitance compared to model② in available range. However, since model③ has narrower width and gap between adjacent wire, once

the thickness of sensitive layer is about  $20\mu\text{m}$  resulting in the geometric parameter  $r$  close to 1 in terms of model③, there is no more significant effects induced by geometric variable on the total capacitance, which also means sometimes it may have lots of practical limits due to its small configuration, especially in terms of fabrication process we will discuss further.

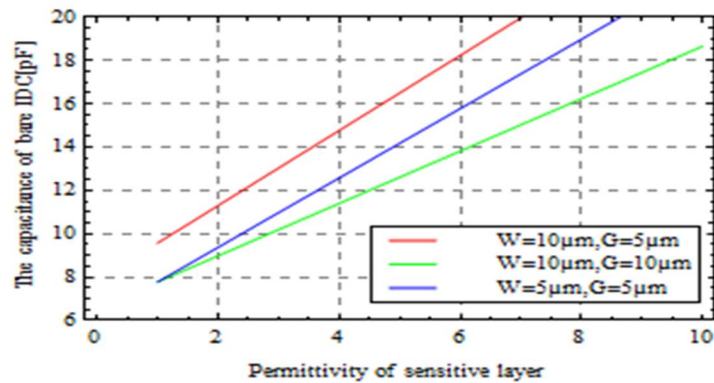


**Fig 4.7 Dependence of capacitance on permittivity of sensitive layer**

In conclusion, corresponding to discussion we made previously and comparing to three models simulated under certain condition, we prefer to have a higher sensitivity and consequently, a large metal ratio  $\eta$  but not too large would be optimum. Although there exists a positive correlation in Fig. 4.4 between metal ratio  $\eta$  and overall capacitance  $C$ , in order to avoid complication during observation and calculation, one would like 0.6~0.8 as the value of  $\eta$  rather than more than 0.9 range. For geometric parameter  $r$ , which is smaller than its saturation value, is desired. On other side, another aspect to take in account is the possibility of the swell of the sensitive layer, which usually happens in polymeric layers when absorption occurs. This swelling can lead to a measurable change in capacitance if the thickness of the sensitive layer is made to have a value far from its saturation value. However, we should know that the effect of change of height of sensitive layer is less significant than the change of permittivity of sensitive layer. In most case, we can

neglect the former corresponding to  $r$ . In our case, we can get a good compromise  $r=0.3$  where the capacitance is not too far from its saturation value but still is sensitive to changes of the permittivity near the surface of the sensitive layer. Therefore, how to choose optimum value of each parameter is not stereotypical, which sometimes need to be done by according to the actual purpose and condition. In our case, considering that one with longer wavelength has much wider detectable area, as shown in Fig. 4.5 and Fig. 4.6, we prefer model①, which has bigger metal ratio and is always sensitive highly to even little change of capacitance.

However, considering the point of view of the production, the model ① with inter spacing of 5  $\mu\text{m}$  will be hard to keep because it makes about 50% of the electrodes to fail during fabrication process although it make the best performance among these three samples. On the other side, model ② also has a reasonable behavior as expected. Through overall consideration, we prefer the model with 10  $\mu\text{m}$  width and 10  $\mu\text{m}$  gap as our design. Fig. 4.8 shows the schematic of capacitor we design consisting of 130 fingers. The geometrical parameters is listed in Table 4.1.

**Table 4.1 The geometrical parameters of the proposed capacitor**

PARAMETER	SYMBOL	VALUE
Finger Width of Capacitor	$W_C$	0.01mm
Finger Gaps of Capacitor	$G_C$	0.01mm
Finger Length of Capacitor	$L_C$	2mm
Number of Fingers	$N_C$	130
The Thickness of Finger	$t$	0.002mm

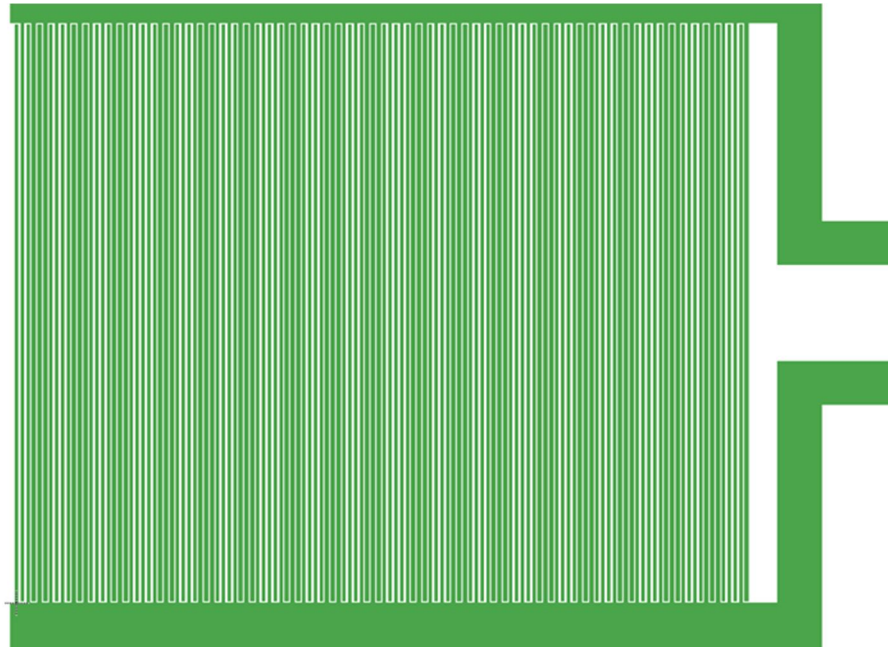


**Fig 4.8 Layout of interdigital capacitor sensing element**

### **4.3 Design of Spiral Inductor**

Spiral inductors, as shown in Fig 4.9, are utilized widely to make resonant circuit elements for capacitive sensors in the microelectronics field. They provide high quality factor elements and are feasible in harsh environment applications.

Coupling the primary reader antenna, as illustrated in Fig. 1.2, the spiral inductor acts as a transformer based on the principle of electromagnetic induction. When an oscillating current is executed on the antenna, a changing magnetic field to both the primary antenna and the spiral inductor is produced along the magnetic path in the air. An alternating voltage of the same frequency is induced in the spiral inductor. The DNA molecule behavior on the top of interdigital capacitor variations induce the frequency change, which can be detected from reader side by monitoring the impedance across the terminals of the wide bandwidth reader antenna. In other

words, the electrical energy is transferred from the input antenna to the sensor and the DNA information can be detected by the reader from the coupled magnetic field.

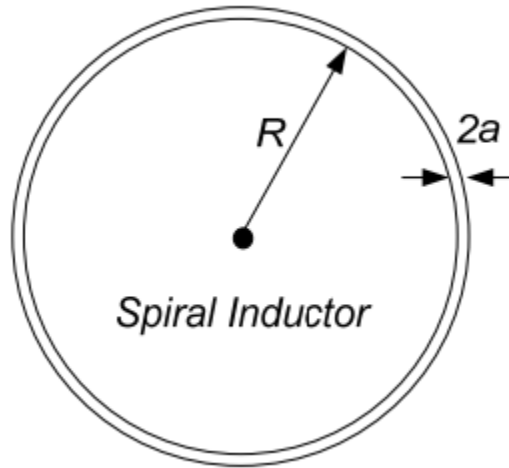


**Fig 4.9 Schematic of Spiral Inductor**

In order to detect DNA immobilization and hybridization, it is necessary to design and fabricate an appropriate spiral inductor to have both a reasonable inductance and high quality factor. Inductance (or electric inductance) is a measurement of the amount of magnetic flux produced for a given electric current. Strictly speaking, this quantity is called self-inductance, because the magnetic field is created solely by the conductor that carries the current. The self-inductance of a straight conductor of length,  $l$ , and radius,  $a$ , (neglecting the effects of nearby conductors), is given by [55].

$$L \approx \frac{\mu_0 l}{2\pi} \left[ \ln \left( \frac{2l}{a} \right) - 0.75 \right] \quad (4.3)$$

Here the magnetic permeability of free space,  $\mu_0$ , is  $4\pi \times 10^{-7}$  H/m. Different types of spiral inductors have respective calculation equations according to [56]. However, there is no closed-form solution for the inductance of circular loops. The self-inductance of a circular loop of round wire, as shown in Fig. 4.9 has a low frequency inductance that can be estimated according to equation 4.4 [55]:

$$L \approx n^2 \mu_0 R \left[ \ln \left( \frac{8l}{a} \right) - 1.75 \right] \quad (4.4)$$

Here the loop radius is R, the wire radius is a, and n corresponds to the turns of the inductor. Fig. 4.10 indicates how the coil turn and inductor radius affect inductance, for a wire radius a yielding to 0.337mm.

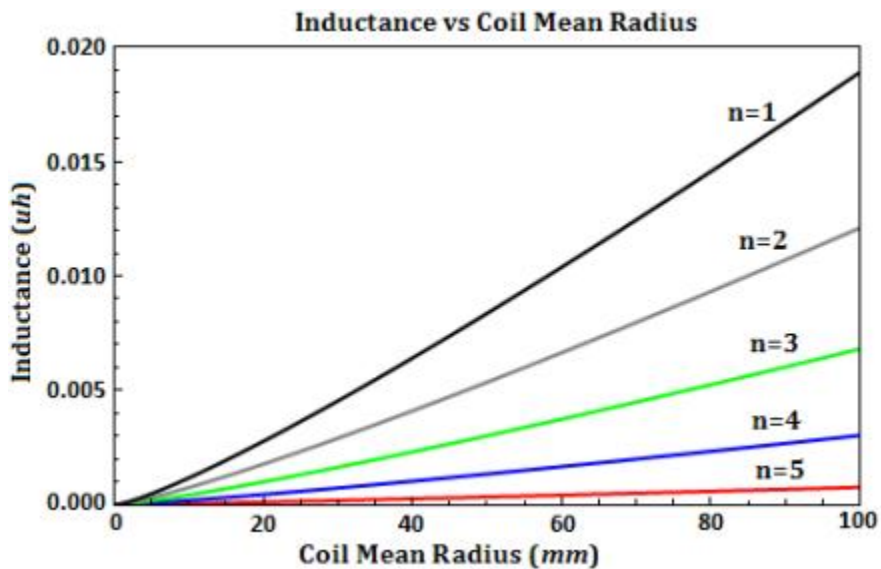


**Fig 4.10 Inductance vs. Coil Mean Radius**

## 4.4 Sensor Performance

### 4.4.1 Electrical Model of Resonant Circuit

The planar inductor coil, together with the interdigital capacitor electrodes, forms a planar structure that has an integrated passive resonant circuit. The simplified model of the series connected PI and IDC with a nearby reader coil for inductive powering is illustrated in Figure 4.11 where the sensor's theoretical electrical model as well as the reader coil used for inductive powering is represented by a parallel plate capacitor  $C_S$ ; inductor  $L_S$ ; the resistance existing in the reader side  $R_R$ ; the resistance in the sensor circuit  $R_S$ ; a time variant current  $I_1$  which enables the resonant frequency to vary in time with a given interval  $T$ ; the capacitance of the reader circuit  $C_R$  that is used to maximize the current applied through the reader antenna; and the mutual inductance  $M$ . The frequency of this current  $\omega$ , is a linear function with respect to time and can be given by (4.5):

$$\omega = \Delta\omega \cdot t + \omega_0 \quad (T \leq t \leq T + \Delta t) \quad (4.5)$$

Once the current with a varying frequency applied to the primary coil, a varying magnetic field generated around this coil. Based on Faraday's law, induced voltage is generated on the remotely placed sensor.

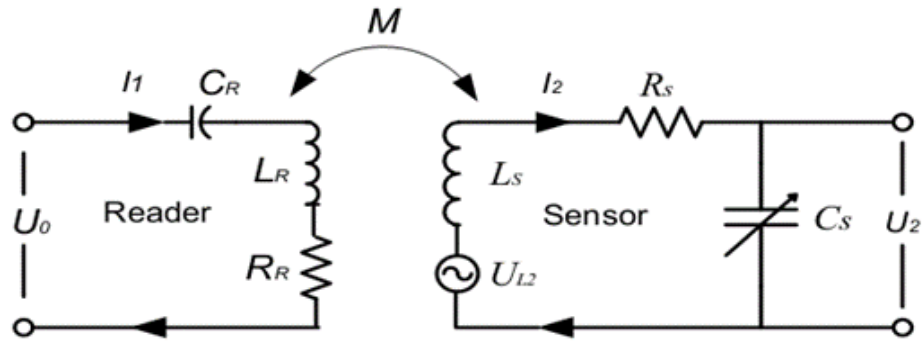


**Fig 4.11 Inductively Coupled Circuit**

If  $U_{L2}$  indicates the voltage induced in the sensor inductor, it can be calculated by equation (4.6):

$$U_{L2} = j\omega M I_1 \quad (4.6)$$

The voltage  $U_2$  on the capacitor of the sensor can be expressed as follows [48]:

$$U_2 = U_{L2} - j\omega L_2 I_2 - R_S I_2 \quad (4.7)$$

And the current is determined by equation (4.8):

$$I_2 = j\omega C_S U_2 \quad (4.8)$$

Therefore, by solving Equation (4.7) and (4.8), the voltage across the planar capacitor  $U_2$  becomes

$$U_2 = \frac{U_{L2}}{1 + (j\omega L_S + R_S) j\omega C_S} \quad (4.9)$$

When this planar resonance sensor is placed in the time-variant magnetic field of the reader antenna  $L_R$ , the voltage  $U_{L2}$  will be induced between the inductor of the sensor. Once the capacitance of the sensor changed according to the behavior of DNA,  $U_2$  will change accordingly and then a change is detected in the voltage  $U_0$  across the reader.

The voltage response of the reader's antenna coil versus sweep frequency without the present of a sensor can be calculated by

$$U_0 = (j\omega L_R + R_R + \frac{1}{j\omega C_R}) \cdot I_1 \quad (4.10)$$

And the voltage response of the reader's antenna coil versus sweep frequency with the present of a sensor can be calculated by

$$U_0 = \left( j\omega L_R + R_R + \frac{\omega^2 k^2 L_R L_S}{j\omega L_S + R_S + \frac{1}{j\omega C_S}} \right) \cdot I_1 \quad (4.11)$$

Where  $k$  is called coupling coefficient defined by Equation (4.12)

$$k = \frac{M}{\sqrt{L_R L_S}} \quad (4.12)$$

The idea above means that the capacitance change at a certain frequency is measured as variation of voltage. However, this change in voltage  $U_0$  is too insignificantly small to measure (see equation (4.10), (4.11)). In the analysis of the influence of the sensor on the frequency

response of  $V_0$  across the reader antenna, the classical approach is to eliminate the coupled reader coil and the sensor by reflecting impedances back to the reader. Since the capacitance variation will change the resonant frequency ( $f_0$ ) of the planar resonator, usually a signal is used to generate a periodical sweep in frequency around the sensor's natural frequency to measure the frequency variation, rather than measuring the voltage variation at a certain frequency. Therefore, the frequency response of  $U_0$  on the reader coil is measured to monitor the reflected impedance  $Z_S'$  change due to the capacitance ( $C_S$ ) variation on the sensor. In this way, a very small variation in the impedance can be measured. The total impedance  $Z_0$  of the series resonant circuit of reader with the inductive coupled sensor can be calculated.

$$Z_0 = Z_R + Z_S' \quad (4.13)$$

$$Z_S' = \frac{\omega^2 k^2 L_R L_S}{j\omega L_S + R_S + \frac{1}{j\omega C_S}} \quad (4.14)$$

A general resonant circuit is comprised of elements that dissipate energy and store energy: resistive components dissipate energy and reactive components store energy. Stored energy gives rise to a phase shift between the voltages and currents in a system. It is customary to employ complex variables to describe such systems, such that a measured real quantity is in phase with the excitation signal and a measured imaginary value is 90 degrees out of phase with the excitation signal. A positive value of reactance is defined as inductive and a negative value of reactance is defined as capacitive. Any passive circuit has the following properties at resonance:

At resonance, inductive and capacitive reactance are equal in magnitude. Since they are of opposite signs and the tank's equivalent reactance consist of the sum of the individual reactance, they cancel the reactance each other.

Since the reactance vanishes at resonance, the observed impedance of the circuit is purely resistive. Mathematically, this implies that the measured impedance is thus purely real with zero phase shifts.

Provided that the losses in the circuit are small relative to the reactance, the magnitude of the measured voltages and currents shall exhibit a pronounced peak (or dip) in the vicinity of resonance.

The resonant frequency of the sensor indicates the point where the voltage appears as an abrupt change. Generally speaking, the resonant frequency occurs at the peak of the voltage plot during a sweep frequency range as long as the magnitude of inductive reactance equals to capacitive reactance. That is to say:

$$j\omega L_S = \frac{1}{j\omega C_S} \quad (4.15)$$

At that moment, the impedance  $Z$  can be regarded as being purely resistive. The expression of the resonant frequency is defined by the following equation:

$$f_0 = \frac{1}{2\pi\sqrt{L_S C_S}} \quad (4.16)$$

Here  $L_S$  is defined as inductance of sensor and  $C_S$  corresponds to the capacitance in the circuit. As shown in Fig. 4.12, if  $f \gg f_0$ , the impedance of the inductor and the amplitude of voltage on the inductor is much larger than the capacitor. However, if  $f \ll f_0$ , impedance of the inductor and the amplitude of voltage on the capacitor is much larger than the inductor. As long as  $f = f_0$ , the impedance of the system is minimal, the amplitudes of the capacitor and inductor are equal and the circuit is in resonance.

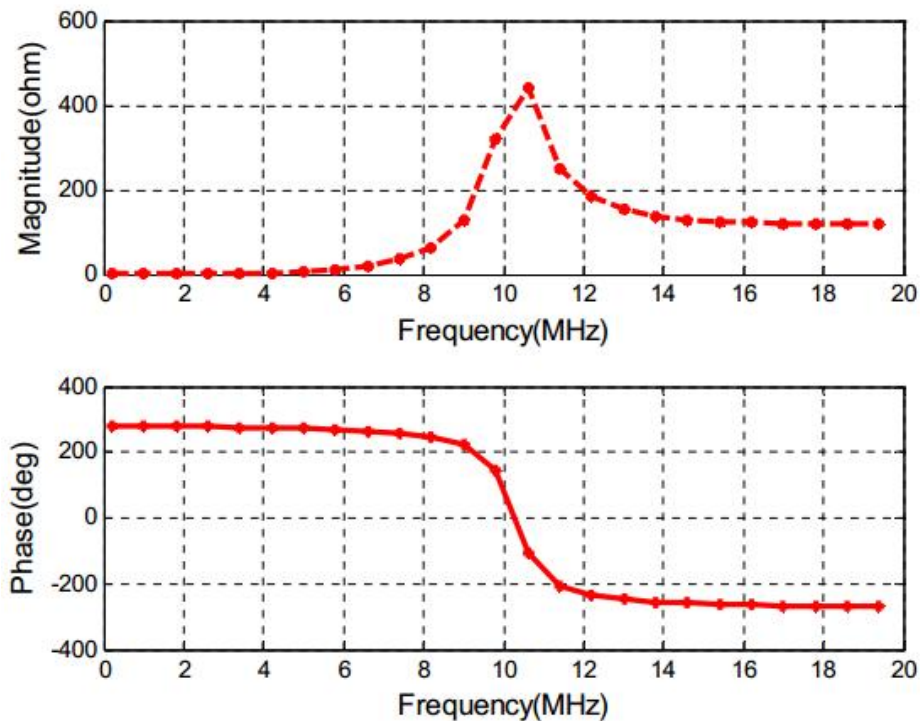


**Fig 4.12 Magnitude & Phase Angle of  $Z_0$**

The figure above shows the magnitude of impedance and phase of this reflected sensor impedance in response to the sweeping frequency changes, the simulation is calculated by the parameter values listed in Table 4.2.

**Table 4.2 System Parameter Values**

Reader Inductance $L_R$	1.5 $\mu$ H
Sensor Inductance $L_S$	0.68 $\mu$ H
Sensor Total Resistance $R_L$	6ohm
Sensor Nominal Capacitance $C_S$	0.24 nF
Nominal Coupling Factor $k$	0.4
Reader Radius $r_R$	30cm
Inductor Radius $r_S$	28.5cm
Coupling Distance $d$	2.5cm

Obviously, this equation shows that minimizing the total resistance and maximizing sensor inductance will improve the Q-factor. However, in our case, increase the turns of the sensor inductor will decrease the  $L_S$  and  $R_S$  simultaneously. In other word, we need know the exact value or expression of resistance in coil and apply Eq. (4.17), so that we can obtain total resistance and evaluate a compromise solution.

$$R_{\text{total}} = \frac{1}{\sum_{i=1}^{npw} R_{\text{wire},i}^{-1}} \quad (4.17)$$

#### 4.4.2 Q Factor

The quality of the LC resonant circuit can be evaluated by Q-factor. Higher Q indicates a lower rate of energy loss relative to the stored energy of the resonator; the oscillations die out more slowly. As usual, Q-factor is used to characterize a resonator' bandwidth relative to its center frequency, which means the higher the Q, the narrower and 'sharper' the peak is. In general, the Q-factor can be defined as the ratio of the total stored energy to dissipated energy per unit cycle in this equation:

:

$$Q = \frac{2\pi f W_{\text{stored}}}{P_{\text{dissipated}}} \quad (4.18)$$

Here,  $W_{\text{stored}}$  is the total stored energy during transmitting of the energy,  $P_{\text{dissipated}}$  is average dissipated power which may be caused by heat consumption of impedance in the circuit.

In order to exhibit a large amplitude response, low internal losses and weak coupling to the external environment are also required. A higher Q-factor indicates a lower rate of energy dissipation relative to the oscillation frequency. Generally, the Q-factor is interpreted as an indication of the sharpness of the resonance peak. The simplified expression of Q-factor is defined by

$$Q = \frac{2\pi f_r L_S}{R_S} = \frac{1}{R_S} \sqrt{\frac{L_S}{C_S}} \quad (4.19)$$

Where  $R_s$  is the total sensor resistance consisting of the inductor resistance, capacitor resistance and circuit resistance.

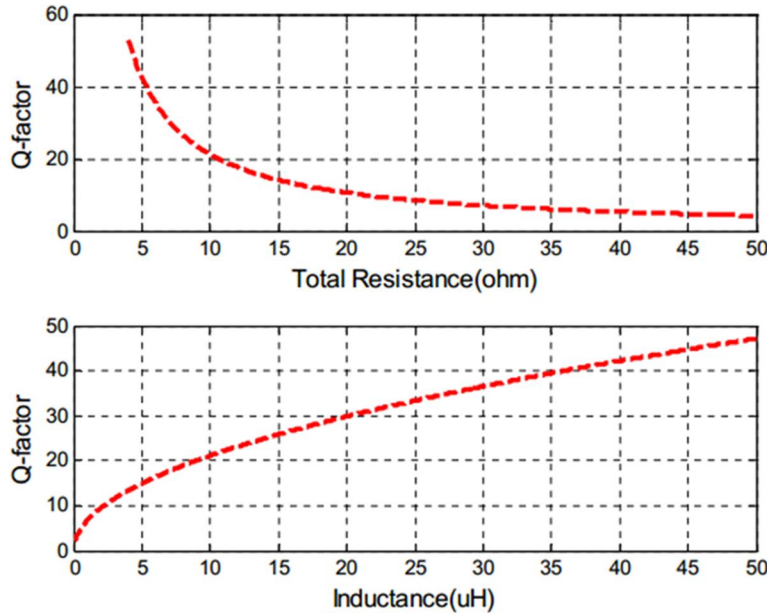


**Fig 4.13 Q-factor vs. Resistance & Inductance**

The fig. 4.13 depicts the variation of the Q-factor with respect to total sensor resistance and sensor inductance for the same nominal value of other parameters as shown in Table 4.2. Obviously, this figure shows that minimizing the total resistance and maximizing sensor inductance will improve the Q-factor.

#### 4.4.3 Coupling Factor

The coupling factor,  $k$ , is used to depict the measurable degree of coupling between adjacent coils. The higher value of  $k$  indicates higher fraction of the flux of the primary that cuts the secondary coil, as shown in Eq. (4.20), which means the lower dissipated flux.

$$k = \frac{M}{\sqrt{L_1 L_2}} = \sqrt{\frac{(M i_1)(M i_2)}{(L_1 i_1)(L_2 i_2)}} = \sqrt{\frac{\varphi_{12} \varphi_{21}}{\varphi_{11} \varphi_{22}}} \leq 1 \quad (4.20)$$

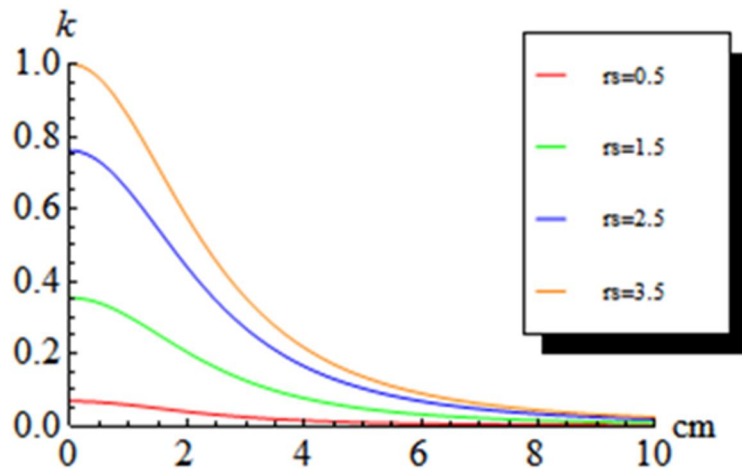
Where  $L_1$ ,  $L_2$  is self-inductance coefficient of coil 1 and 2, respectively;  $M$  is mutual-inductance coefficient between them;  $i_1$ ,  $i_2$  are flow of current to each corresponding coil;  $\varphi_{11} \varphi_{22}$  are self-inductance flux linkage of related coil and  $\varphi_{12}$ ,  $\varphi_{21}$  are mutual-inductance flux of coils. Obviously, the range of  $k$  value is 0~1. Systems are said to be tightly coupled, loosely coupled, critically coupled or overcoupled. Tight coupling is when the coupling coefficient is around 1 as with conventional iron-core transformers. Overcoupling is when the secondary coil is so close that it tends to collapse the primary's field, and critical coupling is when the transfer in the passband is optimal. Loose coupling is when the coils are distant from each other, so that most of the flux misses the secondary, in Tesla coils around 0.2 is used, and at greater distances, for example for inductive wireless power transmission, it may be lower than 0.01[42].

A fair approximation of coupling factor  $k$  with respect to design parameter of the proposed sensor in this study is given by equation (4.21).

$$k = \left( \frac{r_s r_R}{r_R^2 + D^2} \right)^{\frac{3}{2}} \quad (4.21)$$

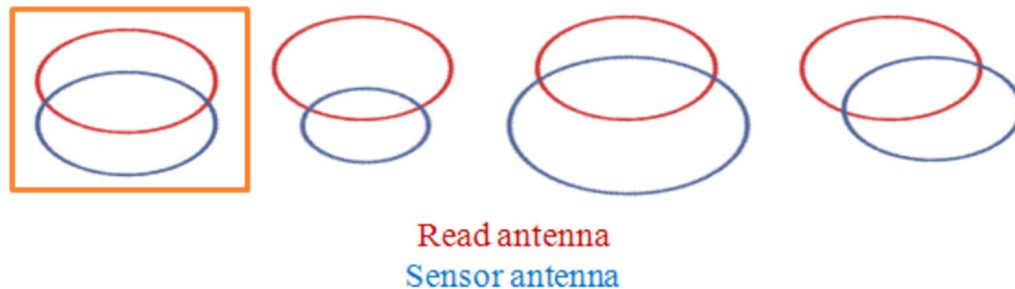
However, this only applies if the  $r_R$  fulfill the condition  $r_s \leq r_R$ . Here,  $r_R$  corresponds to the radius of the primary coil,  $r_s$  indicates the radius of the sensor inductor, and  $D$  is the coupling distance [52].

Fig. 4.14 illustrates how  $r_s$  and  $D$  affect the coupling factor,  $k$ , when  $r_R = 2.5\text{cm}$ . The plot indicates that maximizing the coupling distance and maximizing the radius of sensor will improve the coupling factor.



**Fig 4.14 Coupling factor vs. Length of radius of sensor,  $r_s$  (cm), with different  $r_R$**

Therefore, Close inspection of the Fig. 4.15 suggests that when the radius of the sensor inductor is equal to the radius of the reader antenna, we will get the maximum coupling factor  $k$ .



**Fig 4.15 Radius of the sensor inductor design result**

## 4.5 Conclusions

In this chapter, DNA capacitive sensing principle, planar spiral inductor of the sensor and electrical model of the resonant circuit is presented. The key characteristic sensor performance factor such as Q-factor and coupling factor with respect to design parameter has been analyzed. In order to achieve high performance wireless system, characterized with a high Q-factor and a maximized communication distance, one should seek maximizing sensor inductance and radius of sensor inductor while minimizing the sensor resistance, the coupling distance. The spiral inductor with 5 turns was made of copper wire leads and connected to the electrodes of the capacitor. The diameter of the round copper wire was 0.674 mm and the radius of the inductor was 3.1cm as shown in Fig. 4.16.

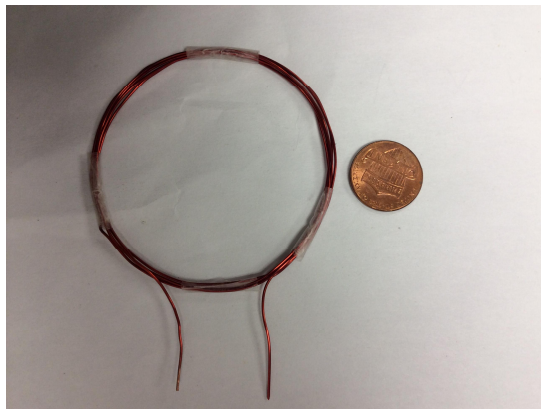


**Fig 4.16 The home made inductor**

## 5 SENSOR CHARACTERIZATIONS

In this chapter, a brief description of the experiment preparation will be presented. In addition, before the novel parallel-connection structure inductor is introduced, a proof of concept experiment should be carried out to verify this completely one-plane coil would replace conventional one. Moreover, a dummy circuit test will be performed to show that this sensing system can measure the resonant frequency change due to presence of capacitance alteration and DNA molecule measurement will be discussed subsequently.

### 5.1 Experiment Preparation

#### 5.1.1 Impedance Principles

Impedance is an important parameter used to characterize electronic circuits, components, and the materials used to make components [11]. It can be defined as the total opposition a device or circuit offers to the flow of an alternated current at a given frequency. Impedance is represented as a complex quantity in a vector plane which graphically has a real part and an imaginary part shown in figure 5.1.

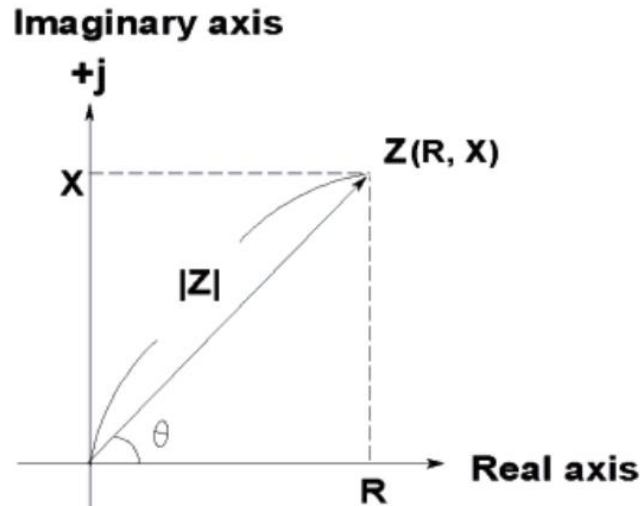
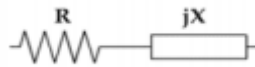


**Fig 5.1 Vector plane with imaginary part (X) and real part (R) [13]**

Impedance can be expressed in the rectangular coordinates form  $R + jX$  or in the polar form  $|Z| e^{j\theta}$ . The imaginary and real axis can be graphically expressed in figure 5.2 as the complex impedance for resistance/inductance or resistance/capacitance combinations. The more ideal an inductor or a capacitor the less resistive a device under test will be, therefore the angle will be close to +90 degrees or -90 degrees [12, 13]. The impedance circuit and mathematical expression of the imaginary impedance can be represented as:



$$Z = R + \frac{1}{2\pi f C j} \quad (5.1)$$

Which include the capacitance, frequency and angular frequency of it. In the circuit representation the imaginary part can be the inductance or capacitance.

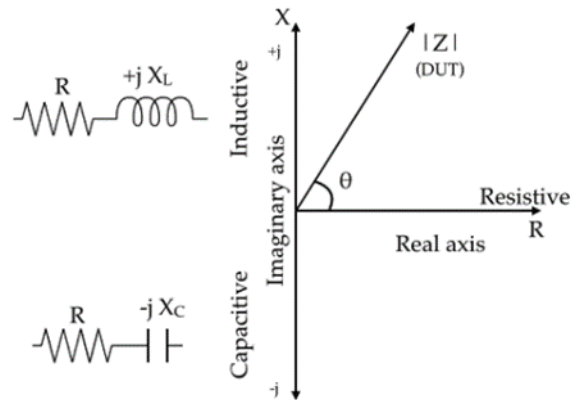


**Fig 5.2 Impedance measurement vector plane representation of a LCR/impedance measurement plane [13]**

### 5.1.2 Experiment Materials

Trizma® base (Lot #SLBF1333V), Sodium phosphate monobasic Reagent Plus®,  $\geq 99.0\%$  (Lot #070M0055V), Potassium pyrophosphate 97% (Lot #MKBP0251V), Potassium ferricyanide (III), powder,  $< 10$  micron, 99+% (Lot #13325DE), Silver cyanide (Lot #MKBH8147V), Thioglycolic Acid (TGA), 1-ethyl-3-(3-dimethylaminopropyl) carbodiimide hydrochloride (EDC), N-hydroxysulfosuccinimide (sulfo-NHS), Potassium ferrocyanide (II) trihydrate Reagent Plus®,  $\geq 98.5\%$  and Iron Chloride (III) Reagent grade, 97% were obtained from Sigma-Aldrich.

Hydrogen Peroxide 30% in water (Lot #140732), Hydrochloric Acid (Lot #130208), Sodium Hydroxide (Lot #090066), Sulfuric Acid OPTIMA (Lot #3212050) and Potassium cyanide (KCN) ACS reagent,  $\geq 96.0\%$  were supplied by Fisher Scientific. Magnesium Sulfate Heptahydrate (Lot #134566) and Potassium Chloride (Lot #126084) were obtained from Fisher BioReagents®.

The ssDNA probes: Bacillus Anthracis CCG ACG AGG GTT GTC AGA GGA TGC GTC GG to use for indirect modifications, GGC TGC TCC CAA CAG TCT CCT ACG CAG CC for

complementary target and TTA CTA CAA AGG AGT CAC AAC GAT AGT AA applied for Non-complementary were obtained from Integrated DNA Technologies (IDT).

### *5.1.3 Equipment and Instrumentation*

The two potentiostat used were: AutoLab PGSTAT 30 from Eco Chemie B.V. and PotentiostatVMP3 Bio Logic Potentiostat from Science Instruments. The BioSpec-nano UV Spectrophotometer (UV Nanodrop) from Shimadzu Biotech was used to determine the concentration of the probes. The STS Vision 310 Plasma Enhanced Chemical Vapor Deposition (PECVD), Brewer Science CEE 100CB Spin Coater (S-C), SUSS MA6 Mask Aligner (MA), OAI 1000Watt DUV Exposure System and CHA SE-600 Electron Beam Evaporator (EBE) with Cryopump at University of Massachusetts at Amherst were used for the fabrication of the IDAM.

Agilent 4396B Impedance Analyzer and the impedance test kit are the ones used to measure impedance, frequency, and other needed parameter together with the impedance test kit Agilent 43961A (Fig. 5.3). This equipment working in a frequency range of 100 kHz to 1.8 GHz can be used to measure the sensor sensitivity with a wireless measurement technique. On the other hand, for capacitance measurement, a precision LCR meter, the Agilent 4285A (Fig. 5.4) that works on a frequency range of 75 kHz to 30 MHz is applied to measure the sensor sensitivity directly with a specific home-made fixture.

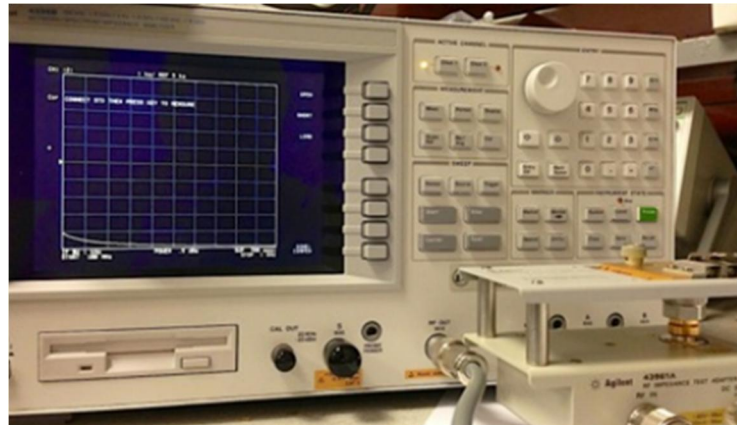


**Fig 5.3 Agilent 4396B setup with impedance test kit Agilent 43961A**



**Fig 5.4 Agilent 4285A Precision LCR meter**

#### *5.1.4 Interdigital Array Microelectrode Preparation*

After fabricated, microelectrodes must be treated in order to be suitable for usage. First they were cut to fit in the sensor connector cable, then washed with a piranha solution for 1 hour to remove any organic residue from the preparation process followed by the passivation layer placement and sealing in the oven at 180°C for 1 hour. For the clearing electrode procedure executed prior to any experiment, several measurements were made in order to optimize the

cleaning parameters. Physical cleaning was done by rinsing the bare electrode with acetone plus isopropanol and drying it with a nitrogen flux. Electrochemical cleaning was performed by cycling at 30 times periods from 0.2 – 1.25 V vs Ag<sup>+</sup>/AgCl at a scan rate of 50 mV/s in a 0.5 M sulfuric acid solution until a reproducible clean gold voltammogram was obtained as Fig. 5.5.

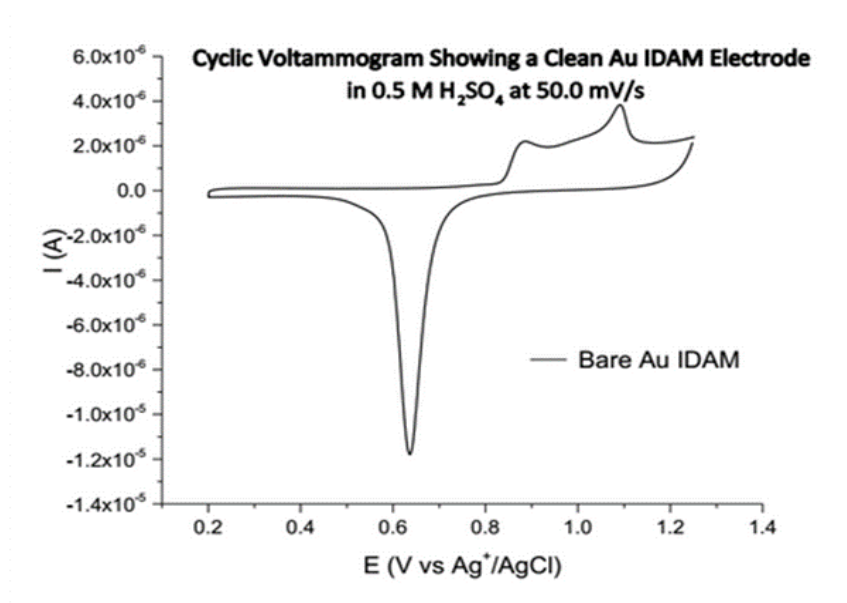


**Fig 5.5 Cyclic Voltammogram for 3 $\mu$ m IDA Au electrode in 0.5 M H<sub>2</sub>SO<sub>4</sub> at 100 mV/s**

### 5.1.5 Preparation of DNA

Single strand of Poly G samples are going to be diluted with 1 mL of nanopure water. Aliquots are going to be transfer to different unit containers and store at 4°C until use. Before use, each aliquot should be deprotected by diluting it with 1.5mL of a dithiothreitol (DTT) 0.4 M solution in 0.17 M phosphate buffer (pH 8.0) and left overnight at room temperature. The aqueous fraction of the deprotected product should be separated and desalted by running it through a size-exclusion NAP-10 column pre-equilibrated with a 0.01M sodium phosphate buffer (pH 6.8). The deprotected

and desalted sample is going to be diluted with Trizma-Na-Mg buffer pH 6.15, to obtain the DNA samples [21].

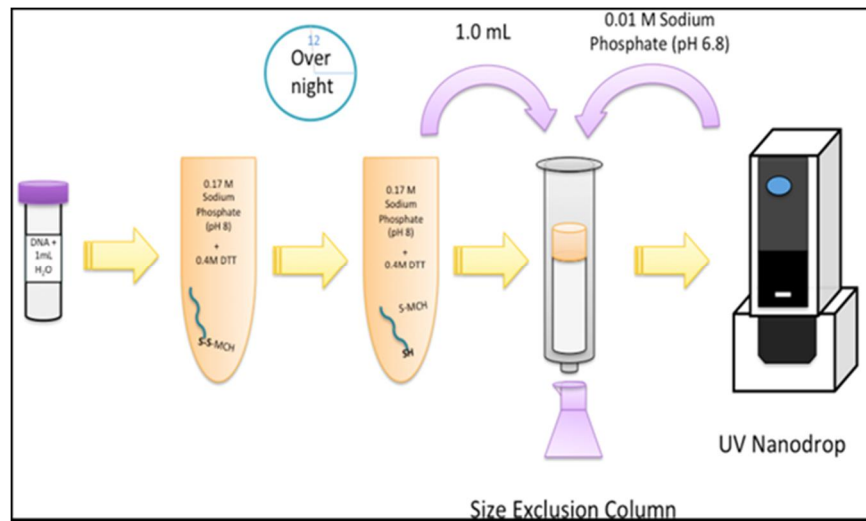


**Fig 5.6 DNA sample preparation process [21]**

### 5.1.6 Proposed Antenna Arrangement for the Impedance Analyzer

In order to have a fixed connection between the wireless measuring fixture of the impedance analyzer and the DNA sensor, an antenna needs to be designed. The connection between the sensor and the antenna needs to be fixed to prevent wire capacitance. Any two wires in a cable can store a charge. This stored charge can affect how the cable behaves during testing [14]. The proposed coil antenna will have 6 turns and the diameter of coil will be 3 inches. This antenna will be connected to a female USB port that will carry the DNA sensor and a second antenna will be connected in the Agilent 16092A Spring Clip Fixture. To assure the female USB connection with the antenna it was used a SMA (SubMiniature version A) coaxial connectors. It was needed to

know how the USB connection behaves related to the sensor chip in order to have the correct contact between them.

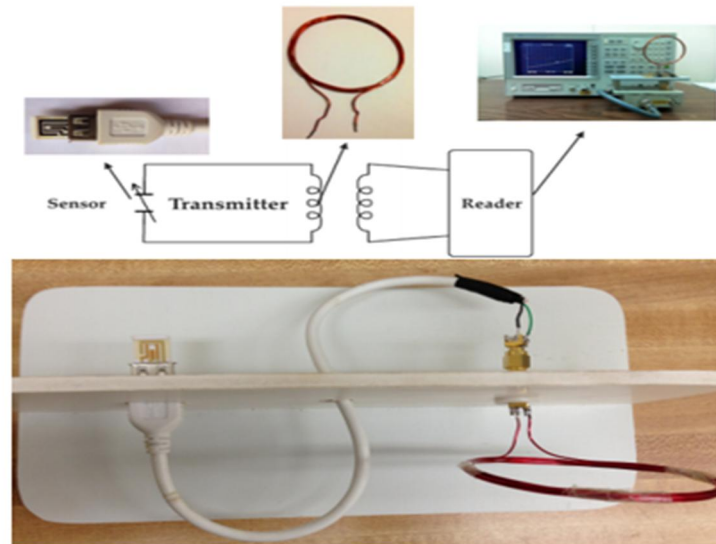


**Fig 5.7 Impedance test antenna arrangement**

## 5.2 Experiment Setup

### 5.2.1 Dummy Test

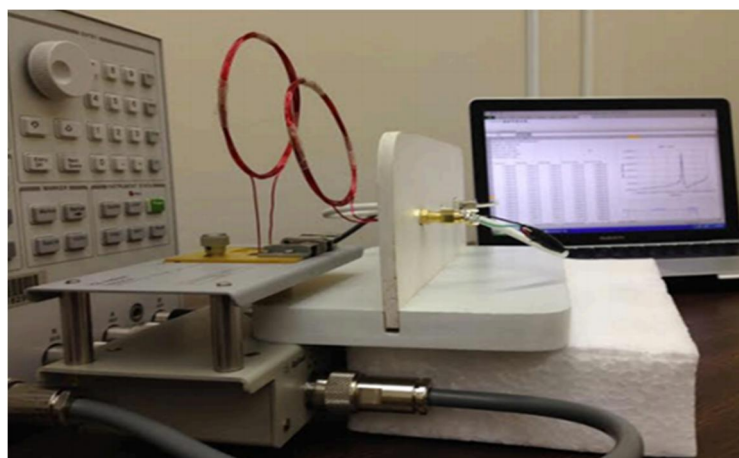


**Fig 5.8 Experimental setup**

In order to verify the proposed antenna arrangement fixture and validate that the resonant frequency will change in response to the varying capacitance, a dummy test would be performed with different known capacitors under the established experiment setup as shown Fig. 5.8. As we expected, the resonant frequency of the sensor defined as the peak point where a sudden change appears in the frequency response of the impedance in every curve increases during the capacitance goes down in Fig. 5.9. The capacitance of bare electrodes is relative small and stable. As long as analyze is deposited, the surface interfacial conformation changes resulting from free charge transmission or varied permittivity constant and consequently the resonant frequency shifts in response of the related capacitance changes. In our experiment, once ssDNA is introduced and immobilized, the capacitance measured should increase theoretically and when the target strand DNA is hybridized probe strand DNA, the relative capacitance is even higher. Consequently, this dummy test offers a reasonable conjecture that the occurrence of the DNA molecule immobilization and hybridization may be witnessed and detected by the frequency peak shifts.

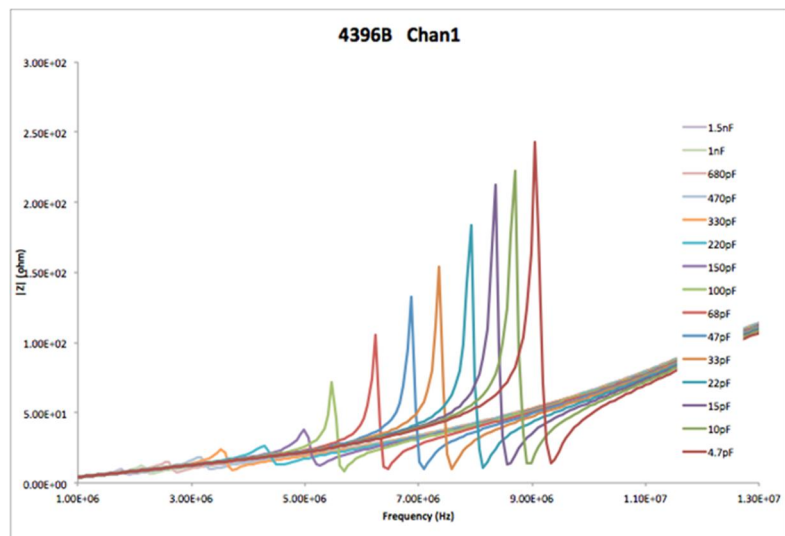


**Fig 5.9 The resonant frequency versus the known-value capacitance**

### 5.2.2 Actual Measuring Test Setup

Proposed interdigital capacitor for calibration is connected to the home-made antenna by female USB port for DNA molecule measurement. Sensor reader separated by a certain distance for wireless data communication and remote power is placed right abreast the sensor (Fig. 5.10). A careful adjustment of the distance between sensor reader and antenna coil was conducted to reach an optimal distance which ensures the efficient the wireless data communication and remote power transfer. The computer software Agilent IO control© is applied for data recording and collecting with a specific cable connected to impedance network analyzer during experiment. Real time monitoring is carried out and the frequency response can be plot out based on EXCEL© while the sensor capacitance varies with respect to the DNA immobilization and hybridization.

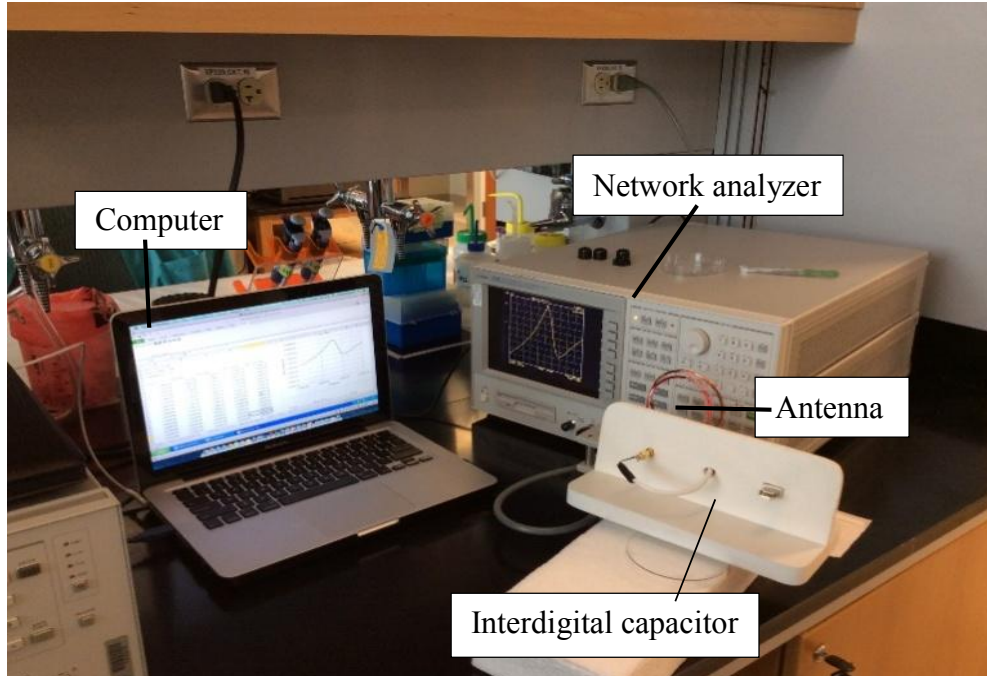


**Fig 5.10 Sensor calibration setup with network analyzer**

For direct capacitance measurement, as shown in Fig. 5.11, all capacitance measurements were performed using a 75 kHz frequency with a test potential of 50 mV. This frequency was selected as a usual range for further readout implementations such as RFID and other wireless RF communication protocols. The potential selected is appropriate for electrochemical studies in biological samples [42]. For each measurement reported the equipment performed an arithmetic average of 64 samples. The related experimental results and system characterization are demonstrated in the next section.

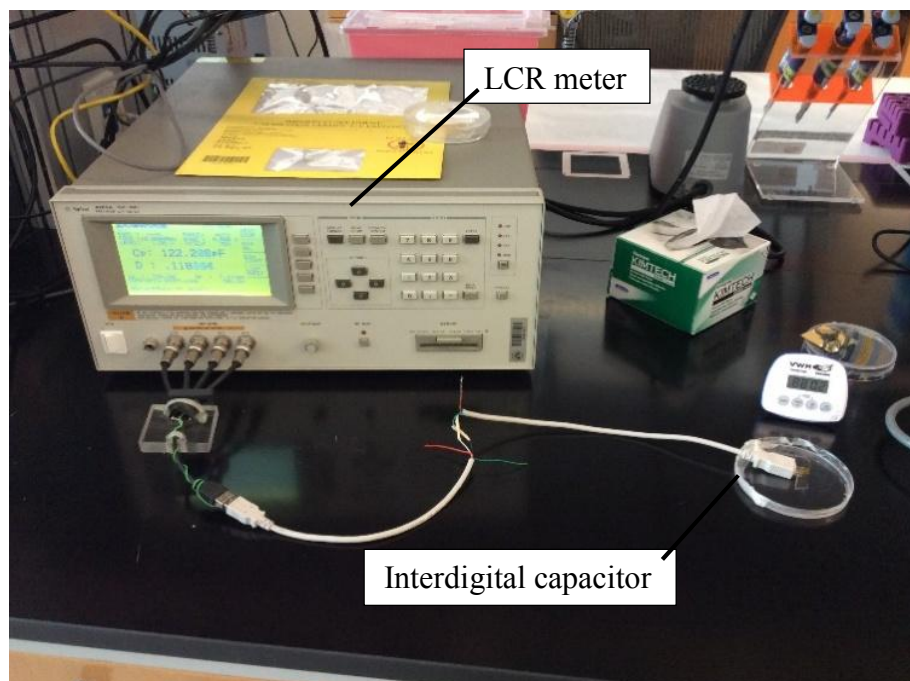


**Fig 5.11 Sensor calibration setup with LCR meter**

## 5.3 Sensor Performances Characterization

### 5.3.1 Experiment Procedure

Step 1 Calibration: Calibration defines the measurement accuracy at the OUTPUT port on the impedance test kit. In terms of its high precision and wide scope, calibration of molecule is much more essential than any other research area. After that, the analyzer can measure within its specified measurement accuracy. Therefore, before introducing specimen, the 0 S, 0  $\Omega$ , and 50  $\Omega$  terminations in the calibration kit are required. In respect to LCR meter, the open and short circuit test were performed leaving an open or short connection between the IDAM connection station docking terminals for eliminating stray capacitance.

Step 2 Baseline measurement: The value of frequency peak is measured and recorded without proposed sensor involved. The measurement is designed to demonstrate the resonant frequency change due to presence of interdigital capacitance.

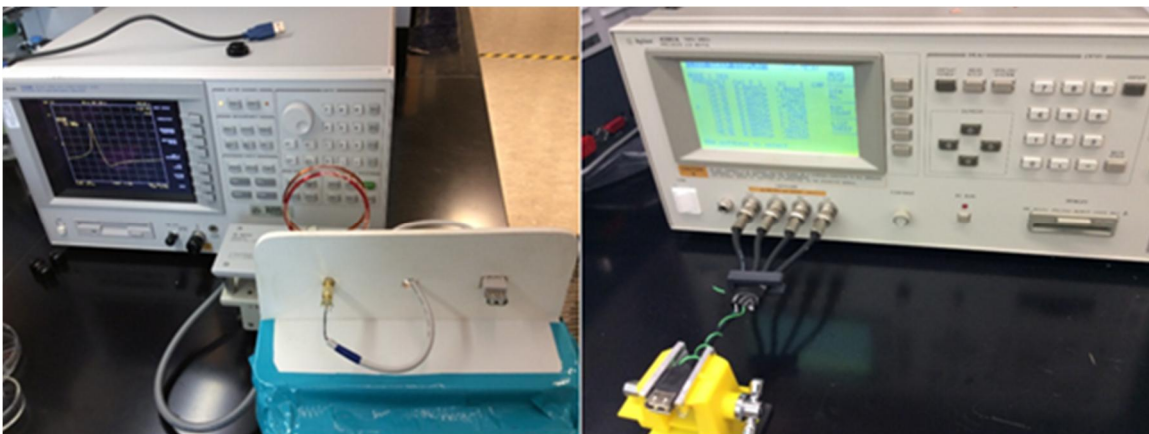


**Fig 5.12 Baseline measurement**

Step 3 Measurement with bare electrodes: The curve peak moved to left in response to IDAM plugged into female USB port as shown in Fig. 5.13. The relevant capacitance increased.

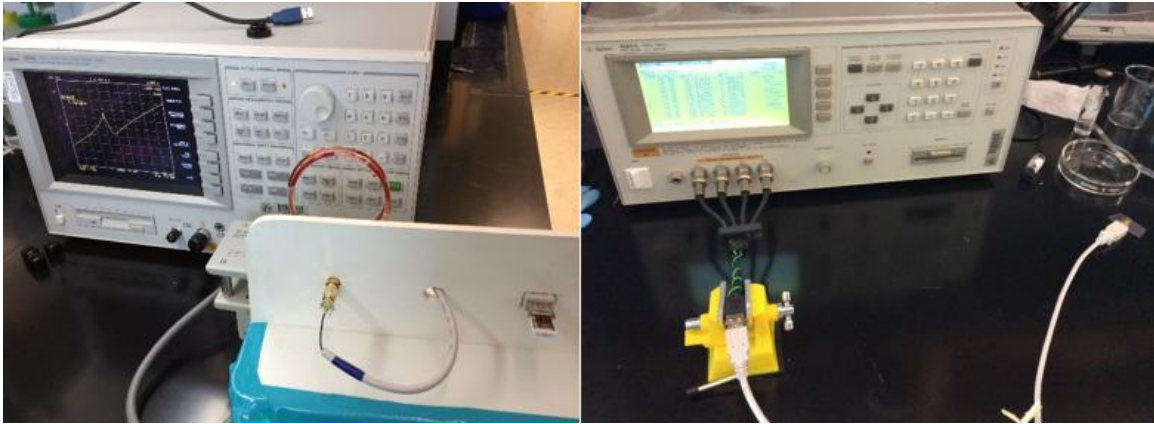


**Fig 5.13 Measurement with bare electrodes**

Step 4 Measurement of ssDNA: Drop of 5 mM ssDNA solution was deposited on the interdigital part enclosed by insulated rubber tape to prevent connection between two electrodes from presence of solution, then kept in a clean petri dish for 20 hours. After of the period is complete, the electrode was rinsed with preparative buffer and dried with a nitrogen stream for eliminating the excess unattached to electrodes. Finally, the frequency peak is observed in network analyzer screen. Also, the capacitance can be obtained by LCR meter readout.

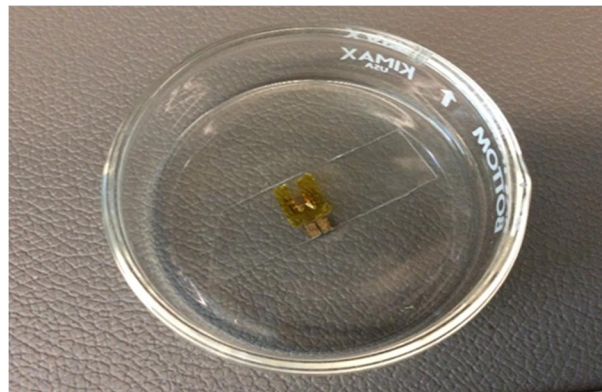


**Fig 5.14 Preparation of ssDNA for immobilization**

Step 5 Measurement of 5mM ssDNA with non-complementary target: After ssDNA molecule was immobilized to electrode surface, non-complementary strand of DNA is introduced and dropped. The cleaning with buffer and nitrogen would be done 3 hours later and following measurement was taken. The measurement is aimed at being a blank experiment for DNA hybridization process.

Step 6 Measurement of 5mM ssDNA with complementary target: Repeat step 5 except for adding the non-complementary strand but complementary one. This step would also take 3 hour and same cleaning task before measurement.

### 5.3.2 Experiment Result

#### 5.3.2.1 Clean IDC capacitance Result

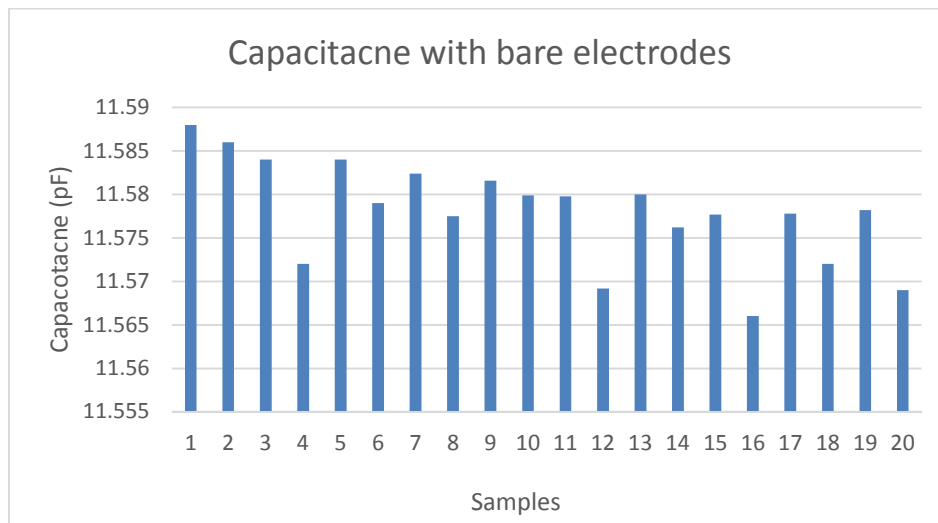


**Fig 5.15 Clean IDAM capacitance in air**

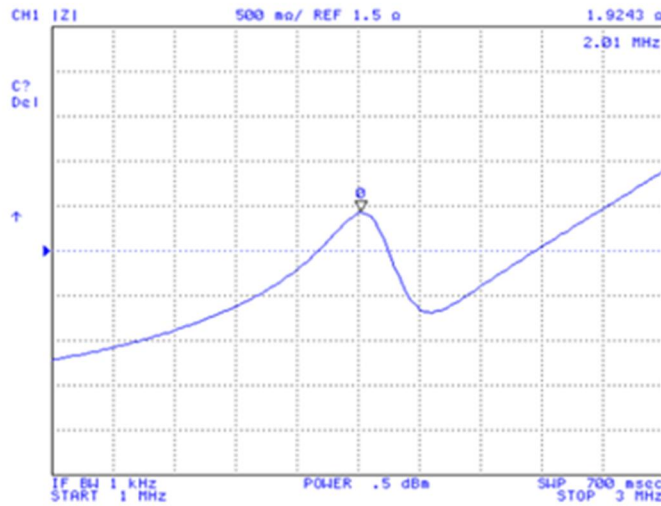


**Fig 5.16 The impedance of bare clean electrodes**

The figures above show the clean IDAM capacitance measurement and the impedance measurement respectively. The average of the performed measurement is 11.58 pF with a resonant frequency 2.01MHz. The theoretical capacitance calculated is 11.76 pF. The difference percentage between both measurements is 1.55%. Fig 5.17 shows the clean IDAM capacitance measurement with the buffer solution on the electrode array. The average capacitance resulted in 337.27 pF.

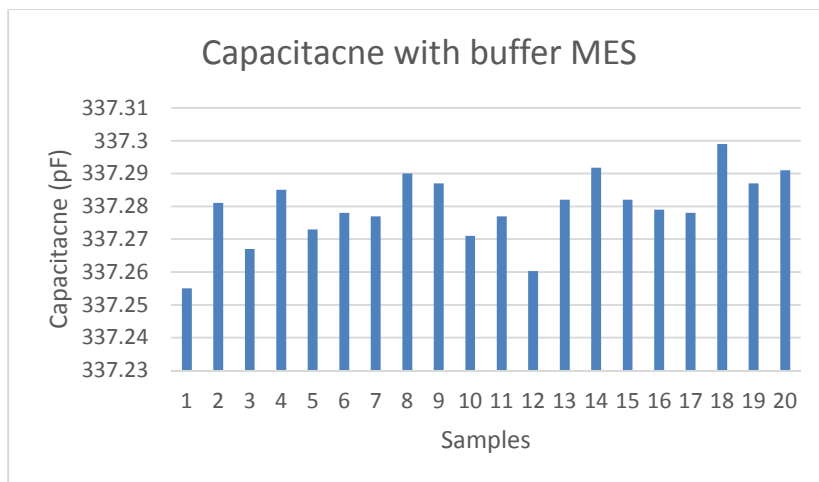


**Fig 5.17 Clean IDAM capacitance in MES buffer solution**

### 5.3.2.2 Immobilization of ssDNA

After the specific strands immobilization period concluded, a MES buffer was placed on the electrode array for removing the residual and Nitrogen stream was applied for drying, then the device capacitance and impedance were again tested as shown in Fig. 5.18 and Fig. 5.19, respectively. The average capacitance resulted in 25.19 pF and 1.97MHz. This presents a capacitance increase of 13.61 pF but a 0.04 MHz decrease of frequency peak over the clean dry IDAM device.

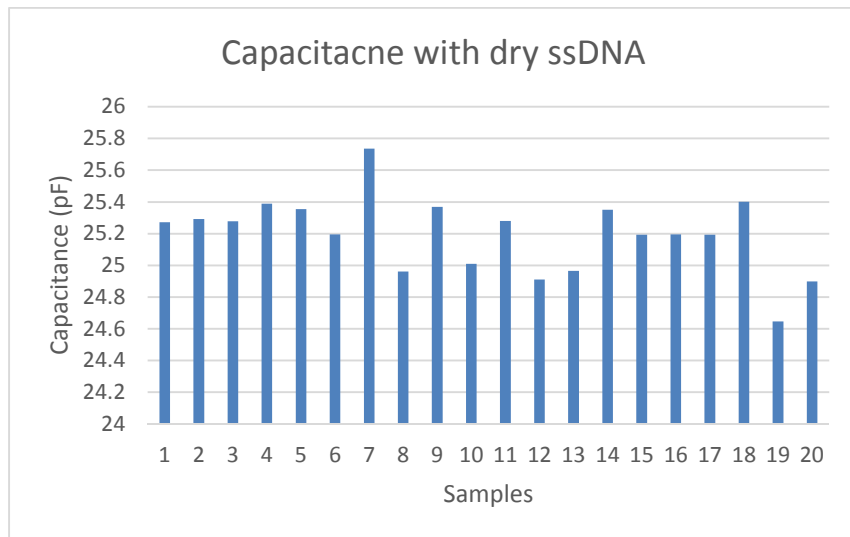


**Fig 5.18 IDAM capacitance after ssDNA immobilization.**

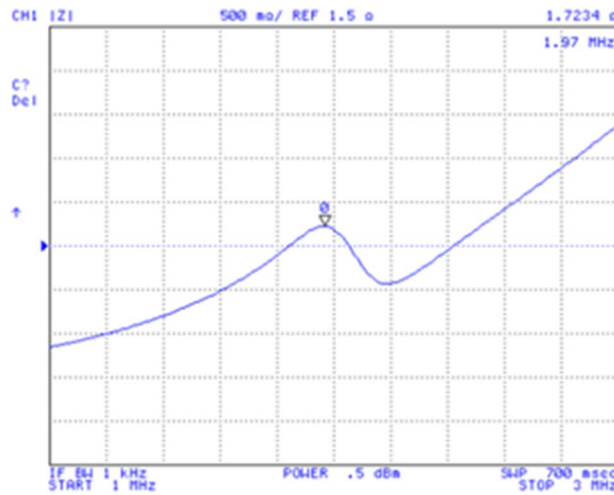


**Fig 5.19 The impedance measurement after ssDNA immobilization**

### 5.3.2.3 Hybridization of the Complementary Strand

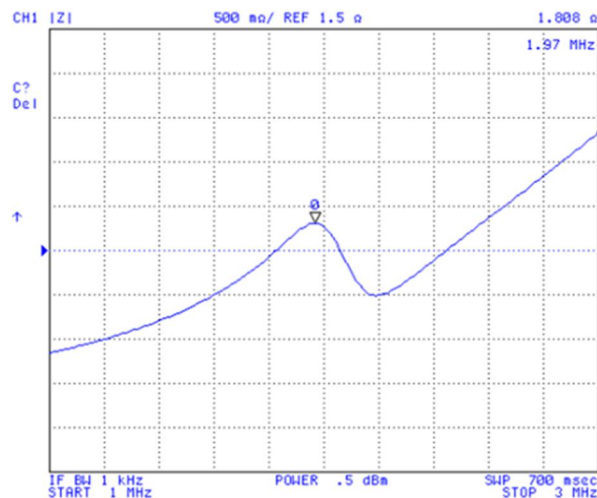


**Fig 5.20 The blank measurement after non-complementary strand**

Before measuring the hybridization of complementary strand, a blank test involving non-complementary strand would be performed. As expected, the impedance peak was stable in 1.97MHz in Fig. 5.20. A MES buffer solution including 5 $\mu$ M of the complementary strand was

placed on the same electrode array, capacitance measurements were taken three hours after the deposition procedure to ensure greater strand hybridization. Fig. 5.21 shows the IDAM capacitance after the hybridization process and Fig. 5.22 for impedance measurement. The hybridization process yielded an average capacitance of 218.6 pF and an average resonant frequency of 1.95MHz. It presents a capacitance increase of 104.1 pF while frequency decreased by 0.02MHz for the hybridization process.

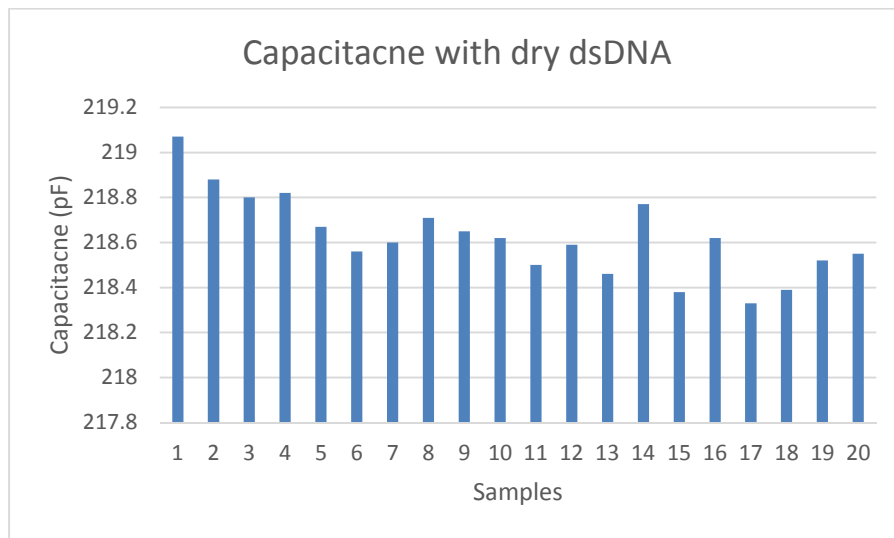


**Fig 5.21 IDAM capacitance after dsDNA hybridization.**

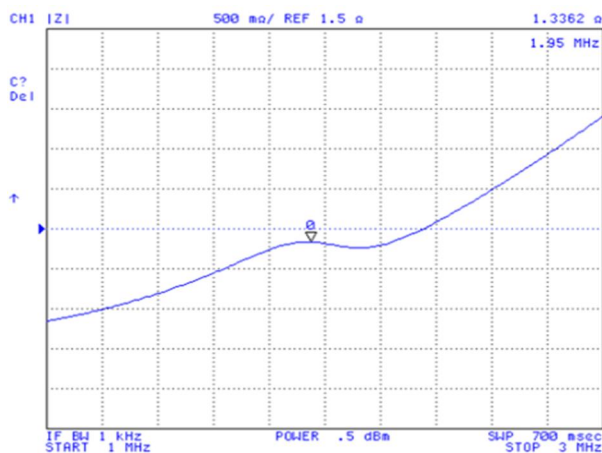


**Fig 5.22 The impedance measurement after complementary strand**

### 5.3.3 Result discussion

Fig. 5.23 shows the capacitance increase after the immobilization and hybridization stage and the frequency peak decrease meanwhile as presented in Fig. 5.24. It is noticeable that each samples is measured and performed an arithmetic average of 32 subsamples.

As illustrated in Fig. 5.23, the capacitance of bare electrodes is relative small. Once the ssDNA is immobilized, the related capacitance increase significantly resulted from free charge interfacial transfer between the ssDNA which carries the negative charge inherently and the electrodes surface. Also, this procedure achieve the energy transfer from DNA molecular energy to electromagnetic energy. The DNA hybridization occurred in the presence of complementary target strand is deposited on the preceding electrodes. It is indicated that the capacitance obtained rise drastically up to 104.1pF since more free charge and energy is presented. The Table 5.1 summarizes the average of capacitance during experiment.

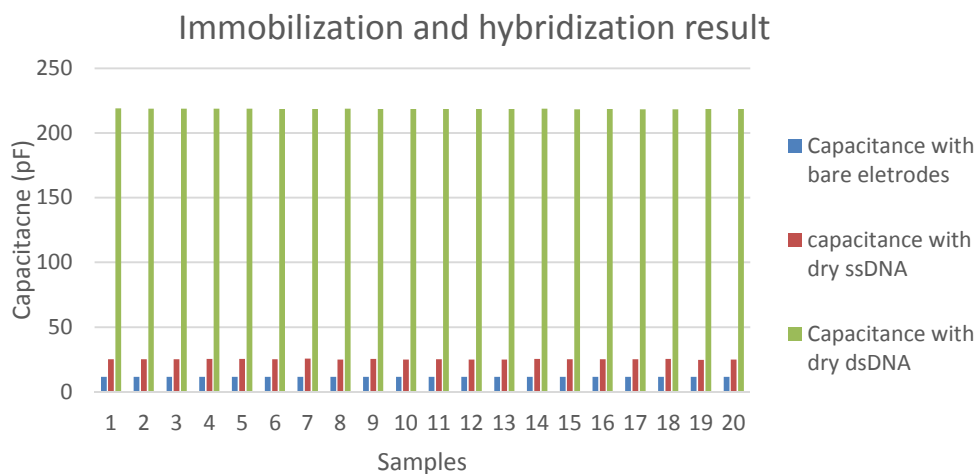


**Fig 5.23 The capacitance measurement after each experiment stage**

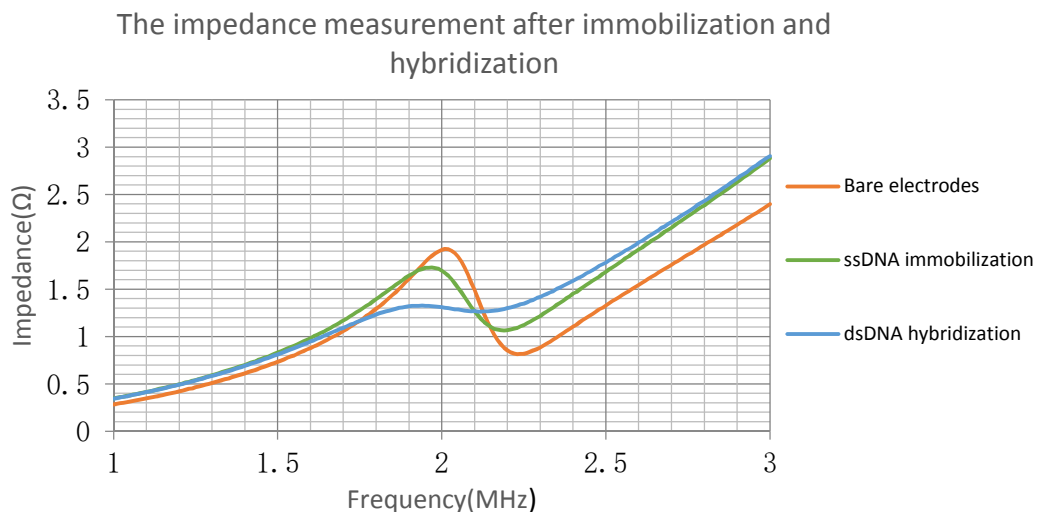
**Table 5.1 Capacitance Change after each Experimental Stage**

Procedure	Capacitance [pF]	$\Delta C$ [pF]
Clean IDC	11.58	/
ssDNA Immobilization	25.19	13.61
dsDNA Hybridization	218.6	104.1

For impedance measurement, the frequency peak changes in response to the presence of DNA as demonstrated in Fig. 5.24. Initially, the frequency point of abrupt change is stable at 2.01MHz, then the ssDNA is used to modify IDC surface, which cause the resonant frequency of the related circuit decreased to 1.97Mz. The measurement following hybridization shows the abrupt point dropped to 1.95MHz based on the relation between capacitacne and resonant frequency in equation (4.16) in previous chapter. Table 5.2 merges the resonant frequency change in each experiment stage.

**Table 5.2 RF Change after each Experimental Stage**

Procedure	Frequency [MHz]	$\Delta f / f$ [%]
Clean IDC	2.01MHz	/
ssDNA Immobilization	1.97MHz	1.99
dsDNA Hybridization	1.95MHz	1.01

**Fig 5.24 The impedance measurement after each experiment stage**

Besides the measurements with dry DNA molecule in this experiment, the capacitance of electrodes is also obtained in buffer MES solution. This measurement followed removing residual DNA with buffer rinse, drying with nitrogen stream and replacing the buffer is accomplished.

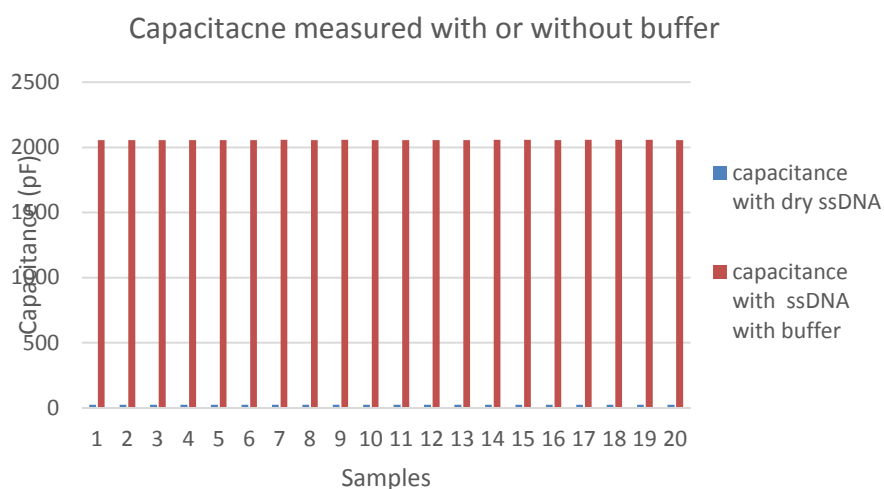


**Fig 5.25 Capacitance measured with or without buffer**

The Fig. 5.25 indicated that DNA molecule immobilization can much more significantly boost the capacitance on electrodes surface measured in buffer than the ones measured after drying with nitrogen stream because of a special structure called electrical double layer that appears on the surface of an object when it is exposed to a fluid. The object might be a solid particle, a gas bubble, a liquid droplet, or a porous body. Double-layer capacitance is the storing of electrical energy by means of the electrical double layer effect [59]. This electrical phenomenon appears at the interface between a conductive electrode and an adjacent liquid electrolyte as observed. By applying a voltage to this electrochemical capacitor, both electrodes generate two layers of polarized ions. One layer of ions is in the surface lattice structure of the electrode. The other layer, with opposite polarity, originates from dissolved and solvated ions distributed in the electrolyte

and has moved in direction of the polarized electrode. Consequently, the capacitance measured in buffer solution is the sum of capacitance among these two layer.

As discussed in previous chapter, besides the geometrical parameters of proposed sensor the permittivity of DNA is also worthy of exploration. However, so far this has remained unknown owing to the lack of experimental techniques able to measure it. Here, we put forwards a tentative method to experimentally determine the dielectric constant of double-stranded DNA. Using the equation (5.1) the permittivity of DNA molecule can be simply calculated by a known value parallel capacitor.

$$C = \frac{\epsilon A}{D} \quad (5.1)$$

Here  $\epsilon$  is the dielectric constant value,  $A$  indicates the electrode plate surface areas,  $D$  is distance between plates.

It is noticeable that while the sequence of DNA may not be affected by your environment, the way genes work—called gene expression—can. The environmental factors such as food, drugs, or exposure to toxins can easily cause epigenetic changes by altering the way molecules bind to DNA or changing the structure of proteins that DNA wraps around. These structural changes can result in slight changes in gene activity; they also can produce more dramatic changes by switching genes on when they should be off or vice versa. Consequently, the capacitance and impedance measurement should be performed and differentiated by specific DNA sequence.

## 6 CONCLUSIONS AND FUTURE WORK

### 6.1 Conclusion

This research project has developed a novel passive wireless DNA molecule sensor, which has the structure with two major parts: a capacitor which is a DNA sensing element and an inductor which works as a passive power source and data communication element. These two components work together as an LC resonator, whose resonant frequency shifts when the capacitance of the sensor changes in response to DNA molecule behavior, to realize the wireless label-free DNA sensing and remote power, eliminating the need for wire connection.

Following the analysis of every geometric factor of LC circuit based on capacitance and inductance modeling and simulation, the sensor configuration was proposed and considerations of design were taken into account. Moreover, the experiment setup and biological methodology was indicated and the experiment procedure was described. The sensor performance was analyzed afterward and the preliminary results denoted a great sensitivity during the DNA molecule immobilization and hybridization. In addition, a novel inductor with parallel-square configuration was developed and showed the huge potential for alternative to conventional spiral planar coil. Finally, the sensor prototype was then successfully fabricated and the fabrication process is introduced as a reference for future research in appendix.

Research contributions achieved by this project can be summarized as follows:

An innovative passive wireless sensor scheme has been successfully demonstrated;

Sensor performance was analyzed;

The sensor prototype was developed and calibrated.

Specifically, the contributions of this research made to the community include:

First of all, the DNA molecule behavior on planar LC sensor has been fully investigated which disclosed a new potential application of the planar resonator to the DNA sensing field in environmental monitoring, biomedical detection, and diagnostic evaluation. These passive wireless sensors can be fabricated at a low-cost so that they are able to be widely used in at point of care such home or clinic. The wireless measurement results of the prototype sensor show a great sensitivity. The proposed DNA bio-sensor provides a simple planar structure and a stable accurate measurement with a passive wireless and reusable feature, which enables a long-term DNA molecule detection and integrated wireless communication.

Secondly, the effective design of planar resonators for wireless sensing applications requires a process to obtain a geometry that optimizes application requirements. Modeling and simulation were performed in order to minimize sensor size, maximize the detection distance, quality factor, and sensor sensitivity.

## **6.2 Future work**

There are couples of researches can be extended as future works, which can be concluded as the follows:

Improve the IDC DNA sensor with higher sensitivity, linearity and minimized sensor size;

Extend the communication distance of the DNA sensor;

Develop a cost-effective way to read out the data transformed from proposed LC circuit, such as applying RFID technology;

Investigate the DNA molecule experiment without limit of specific DNA sequence and molecule concentration;

Explore a feasible monolayer desorption methods to accomplish sensor reusability;

Attempt to figure out a time-saving method to treat the DNA molecule and accelerate DNA immobilization and hybridization.

## References

- [1] Ortiz, P., Jia, Y., Vargas, N., and Cabrera, C., 2013, 'Label-free capacitance DNA sensing', 2013 Seventh International Conference on Sensing Technology (ICST).
- [2] Millan, K., and Mikkelsen, S., 1993, 'Sequence-selective biosensor for DNA based on electroactive hybridization indicators', *Anal. Chem.*, 65(17), pp. 2317-2323.
- [3] Daniels, J., and Pourmand, N., 2007, 'Label-Free Impedance Biosensors: Opportunities and Challenges', *Electroanalysis*, 19(12), pp. 1239-1257.
- [4] Clausen-Schaumann, H., Rief, M., Tolksdorf, C., and Gaub, H., 2000, 'Mechanical Stability of Single DNA Molecules', *Biophysical Journal*, 78(4), pp. 1997-2007.
- [5] Lao, R., Song, S., Wu, H., Wang, L., Zhang, Z., He, L., and Fan, C., 2005, 'Electrochemical Interrogation of DNA Monolayers on Gold Surfaces', *Anal. Chem.*, 77(19), pp. 6475-6480.
- [6] Albers, J., Grunwald, T., Nebling, E., Piechotta, G., and Hintsche, R., 2003, 'Electrical biochip technology? A tool for microarrays and continuous monitoring', *Analytical and Bioanalytical Chemistry*, 377(3), pp. 521-527.
- [7] Clack, N., Salaita, K., and Groves, J., 2008, 'Electrostatic readout of DNA microarrays with charged microspheres', *Nat Biotechnol*, 26(7), pp. 825-830.
- [8] Goodrich, T., Lee, H., and Corn, R., 2004, 'Enzymatically Amplified Surface Plasmon Resonance Imaging Method Using RNase H and RNA Microarrays for the Ultrasensitive Detection of Nucleic Acids', *Anal. Chem.*, 76(21), pp. 6173-6178.
- [9] Cao, Y., 2002, 'Nanoparticles with Raman Spectroscopic Fingerprints for DNA and RNA Detection', *Science*, 297(5586), pp. 1536-1540.

- [10] Bandiera, L., Cellere, G., Cagnin, S., De Toni, A., Zanoni, E., Lanfranchi, G., and Lorenzelli, L., 2007, 'A fully electronic sensor for the measurement of cDNA hybridization kinetics', *Biosensors and Bioelectronics*, 22(9-10), pp. 2108-2114.
- [11] Drummond, T., Hill, M., and Barton, J., 2003, 'Electrochemical DNA sensors', *Nat Biotechnol*, 21(10), pp. 1192-1199.
- [12] Vo-Dinh, T., Alarie, J., Isola, N., Landis, D., Wintenberg, A., and Ericson, M., 1999, 'DNA Biochip Using a Phototransistor Integrated Circuit', *Anal. Chem.*, 71(2), pp. 358-363.
- [13] Liu, T., Tang, J., Han, M., and Jiang, L., 2003, 'A novel microgravimetric DNA sensor with high sensitivity', *Biochemical and Biophysical Research Communications*, 304(1), pp. 98-100.
- [14] Wang, J., 2000, 'SURVEY AND SUMMARY: From DNA biosensors to gene chips', *Nucleic Acids Research*, 28(16), pp. 3011-3016.
- [15] Drummond, T., Hill, M., and Barton, J., 2003, 'Electrochemical DNA sensors', *Nat Biotechnol*, 21(10), pp. 1192-1199.
- [16] Bagni, G., Osella, D., Sturchio, E., and Mascini, M., 2006, 'Deoxyribonucleic acid (DNA) biosensors for environmental risk assessment and drug studies', *Analytica Chimica Acta*, 573-574, pp. 81-89.
- [17] Santiago-Rodríguez, L., Sánchez-Pomales, G., and Cabrera, C., 2010, 'Single-Walled Carbon Nanotubes Modified Gold Electrodes as an Impedimetric DNA Sensor', *Electroanalysis*, 22(4), pp. 399-405.
- [18] Kelley, S., Barton, J., Jackson, N., and Hill, M., 1997, 'Electrochemistry of Methylene Blue Bound to a DNA-Modified Electrode', *Bioconjugate Chem.*, 8(1), pp. 31-37.

- [19] Kerman, K., Ozkan, D., Kara, P., Meric, B., Gooding, J., and Ozsoz, M., 2002, 'Voltammetric determination of DNA hybridization using methylene blue and self-assembled alkanethiol monolayer on gold electrodes', *Analytica Chimica Acta*, 462(1), pp. 39-47.
- [20] Cagnin, S., Caraballo, M., Guiducci, C., Martini, P., Ross, M., SantaAna, M., Danley, D., West, T., and Lanfranchi, G., 2009, 'Overview of Electrochemical DNA Biosensors: New Approaches to Detect the Expression of Life', *Sensors*, 9(4), pp. 3122-3148.
- [21] Chee, M., Yang, R., Hubbell, E., Berno, A., Huang, X., Stern, D., Winkler, J., Lockhart, D., Morris, M., and Fodor, S., 1996, 'Accessing Genetic Information with High-Density DNA Arrays', *Science*, 274(5287), pp. 610-614.
- [22] Lockhart, D., Dong, H., Byrne, M., Follettie, M., Gallo, M., Chee, M., Mittmann, M., Wang, C., Kobayashi, M., Norton, H., and Brown, E., 1996, 'Expression monitoring by hybridization to high-density oligonucleotide arrays', *Nat Biotechnol*, 14(13), pp. 1675-1680.
- [23] Pease, A., Solas, D., Sullivan, E., Cronin, M., Holmes, C., and Fodor, S., 1994, 'Light-generated oligonucleotide arrays for rapid DNA sequence analysis', *Proceedings of the National Academy of Sciences*, 91(11), pp. 5022-5026.
- [24] DeRisi, J., 1997, 'Exploring the Metabolic and Genetic Control of Gene Expression on a Genomic Scale', *Science*, 278(5338), pp. 680-686.
- [25] DeRisi, J., Penland, L., Brown, P., Bittner, M., Meltzer, P., Ray, M., Chen, Y., Su, Y. and Trent, J. 1996, 'Use of a cDNA microarray to analyse gene expression patterns in human cancer', *Nat Genet*, 14(4), pp.457-460.

- [26] Shalon, D., Smith, S., and Brown, P., 1996, 'A DNA microarray system for analyzing complex DNA samples using two-color fluorescent probe hybridization.', *Genome Research*, 6(7), pp. 639-645.
- [27] Prinzen, C., Trümbach, D., Wurst, W., Endres, K., Postina, R., and Fahrenholz, F., 2009, 'Differential gene expression in ADAM10 and mutant ADAM10 transgenic mice', *BMC Genomics*, 10(1), p. 66.
- [28] Guo, J., Miao, Y., Xiao, B., Huan, R., Jiang, Z., Meng, D., and Wang, Y., 2009, 'Differential expression of microRNA species in human gastric cancer versus non-tumorous tissues', *Journal of Gastroenterology and Hepatology*, 24(4), pp. 652-657.
- [29] Sun, X., Li, F., Sun, N., Shukui, Q., Baoan, C., Jifeng, F., Lu, C., Zuhong, L., Hongyan, C., YuanDong, C., Jiazhong, J., and Yingfeng, Z., 2009, 'Polymorphisms in XRCC1 and XPG and response to platinum-based chemotherapy in advanced non-small cell lung cancer patients', *Lung Cancer*, 65(2), pp. 230-236.
- [30] Rivera-Gandía, J., Del Mar Maldonado, M., De La Torre-Meléndez, Y., Ortiz-Quiles, E., Vargas-Barbosa, N., and Cabrera, C., 2011, 'Electrochemical Capacitance DNA Sensing at Hairpin-Modified Au Electrodes', *Journal of Sensors*, 2011, pp. 1-6.
- [31] Sasindran, S., and Torrelles, J., 2011, 'Mycobacterium Tuberculosis Infection and Inflammation: what is Beneficial for the Host and for the Bacterium?', *Front. Microbio.*, 2.
- [32] Smith, I., 2003, 'Mycobacterium tuberculosis Pathogenesis and Molecular Determinants of Virulence', *Clinical Microbiology Reviews*, 16(3), pp. 463-496.
- [33] Read, T., Peterson, S., Tourasse, N., Baillie, L., Paulsen, I., Nelson, K., Tettelin, H., Fouts, D., Eisen, J., Gill, S., Holtzapple, E., Økstad, O., Helgason, E., Rilstone, J., Wu, M., Kolonay, J.,

Beanan, M., Dodson, R., Brinkac, L., Gwinn, M., DeBoy, R., Madpu, R., Daugherty, S., Durkin, A., Haft, D., Nelson, W., Peterson, J., Pop, M., Khouri, H., Radune, D., Benton, J., Mahamoud, Y., Jiang, L., Hance, I., Weidman, J., Berry, K., Plaut, R., Wolf, A., Watkins, K., Nierman, W., Hazen, A., Cline, R., Redmond, C., Thwaite, J., White, O., Salzberg, S., Thomason, B., Friedlander, A., Koehler, T., Hanna, P., Kolstø, A., and Fraser, C., 2003, 'The genome sequence of *Bacillus anthracis* Ames and comparison to closely related bacteria', *Nature*, 423(6935), pp. 81-86.

[34] Stöckel, S., Meisel, S., Elschner, M., Rösch, P., and Popp, J., 2012, 'Raman Spectroscopic Detection of Anthrax Endospores in Powder Samples', *Angew. Chem. Int. Ed.*, 51(22), pp. 5339-5342.

[35] Alley, G., 1970, 'Interdigital Capacitors and Their Application to Lumped-Element Microwave Integrated Circuits', *IEEE Transactions on Microwave Theory and Techniques*, 18(12), pp. 1028-1033.

[36] Hoffmann, R., and Howe, H., 1987, *Handbook of microwave integrated circuits*, Artech House, Norwood, MA.

[37] Wei, J., 1977, 'Distributed capacitance of planar electrodes in optic and acoustic surface wave devices', *IEEE J. Quantum Electron.*, 13(4), pp. 152-158.

[38] Herczfeld, P., 1990, *Special issue on applications of lightwave technology to microwave devices, circuits, and systems*, IEEE, New York, NY.

[39] Huey-Daw Wu, Zhihang Zhang, Barnes, F., Jackson, C., Kain, A., and Cuchiaro, J., 1994, 'Voltage tunable capacitors using high temperature superconductors and ferroelectrics', *IEEE Transactions on Applied Superconductivity*, 4(3), pp. 156-160.

- [40] Kotani, K., Kawayama, I., and Tonouchi, M., 2002, 'Dielectric Response of c -Oriented SrBi<sub>2</sub>Ta<sub>2</sub>O<sub>9</sub> Thin Films Observed with Interdigital Electrodes', *Japanese Journal of Applied Physics*, 41(Part 1, No. 11B), pp. 6790-6792.
- [41] VEYRES, C., and FOUAD HANNA, V., 1980, 'Extension of the application of conformal mapping techniques to coplanar lines with finite dimensions', *International Journal of Electronics*, 48(1), pp. 47-56.
- [42] Mamishev, A., Sundara-Rajan, K., Fumin Yang, Yanqing Du, and Zahn, M., 2004, 'Interdigital sensors and transducers', *Proc. IEEE*, 92(5), pp. 808-845.
- [43] Endres, H., and Drost, S., 1991, 'Optimization of the geometry of gas-sensitive interdigital capacitors', *Sensors and Actuators B: Chemical*, 4(1-2), pp. 95-98.
- [44] Igreja, R., and Dias, C., 2004, 'Analytical evaluation of the interdigital electrodes capacitance for a multi-layered structure', *Sensors and Actuators A: Physical*, 112(2-3), pp. 291-301.
- [45] Casalini, R., Kilitziraki, M., Wood, D., and Petty, M., 1999, 'Sensitivity of the electrical admittance of a polysiloxane film to organic vapours', *Sensors and Actuators B: Chemical*, 56(1-2), pp. 37-44.
- [46] Igreja, R., and Dias, C., 2011, 'Extension to the analytical model of the interdigital electrodes capacitance for a multi-layered structure', *Sensors and Actuators A: Physical*, 172(2), pp. 392-399.
- [47] Ghione, G., and Goano, M., 2003, 'Revisiting the partial-capacitance approach to the analysis of coplanar transmission lines on multilayered substrates', *IEEE Transactions on Microwave Theory and Techniques*, 51(9), pp. 2007-2014.

- [48] Balakrishnan, A., Palmer, W., Joines, W., and Wilson, T., 1992, 'Inductance of planar rectangular-spiral strip conductors for low-profile inductors', PESC '92 Record. 23rd Annual IEEE Power Electronics Specialists Conference.
- [49] Peters, C., and Manoli, Y., 2007, 'Improved and Accelerated Analytical Calculation Algorithm for Multi-Wire Coils to Power Wireless Sensor Systems', TRANSDUCERS 2007 - 2007 International Solid-State Sensors, Actuators and Microsystems Conference.
- [50] Peters, C., and Manoli, Y., 2008, 'Inductance calculation of planar multi-layer and multi-wire coils: An analytical approach', Sensors and Actuators A: Physical, 145-146, pp. 394-404.
- [51] Endres, H., and Drost, S., 1991, 'Optimization of the geometry of gas-sensitive interdigital capacitors', Sensors and Actuators B: Chemical, 4(1-2), pp. 95-98.
- [52] Finkenzeller, K., 2003, RFID handbook, Wiley, Chichester, England.
- [53] Wang, J., 2006, Analytical electrochemistry, Wiley-VCH, Hoboken, N.J.
- [54] Mosbach, K., 1980, 'Immobilized enzymes', Trends in Biochemical Sciences, 5(1), pp. 1-3.
- [55] Snyder, J., and Grover, F., 1964, 'Inductance Calculations Working Formulas and Tables', Mathematics of Computation, 18(85), p. 164.
- [56] Mohan, S., Del Mar Hershenson, M., Boyd, S., and Lee, T., 1999, 'Simple accurate expressions for planar spiral inductances', IEEE J. Solid-State Circuits, 34(10), pp. 1419-1424.
- [57] Kidner, N., Meier, A., Homrighaus, Z., Wessels, B., Mason, T., and Garboczi, E., 2007, 'Complex electrical (impedance/dielectric) properties of electroceramic thin films by impedance spectroscopy with interdigital electrodes', Thin Solid Films, 515(11), pp. 4588-4595.

[58] Smith, W., Gerard, H., Collins, J., Reeder, T., and Shaw, H., 1969, 'Analysis of Interdigital Surface Wave Transducers by Use of an Equivalent Circuit Model', IEEE Transactions on Microwave Theory and Techniques, 17(11), pp. 856-864.

[59] Yamashiro, S., and Nakamura, K., 2012, 'Equivalent circuit model for electric double layer capacitors and its applications', Electrical Engineering in Japan, 180(4), pp. 29-37.

## Appendix A. Novel Planar Inductor

In this appendix, we will put forward a novel configuration of coil as alternative inductor element of the proposed LC sensor, then the analytical calculation will be presented. It indicates that the inductor with proposed distinctive structure has some inevitable advantages compared with traditional planar spiral one, however any experiments have yet to prove its practicability.

### A.1 The Analytical Calculation of Planar Inductor

Amount of publications has illustrated planar inductors with distinct structure. It is particularly worth mentioning here that spiral inductors are widely utilized to make resonant circuit elements for capacitive sensors in the microelectronics field as a result of that they provide high quality factor elements and are feasible in harsh environment applications.

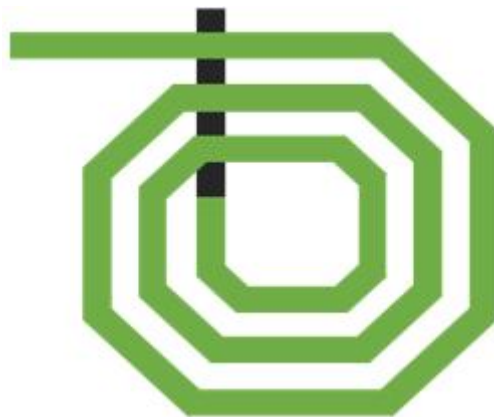


**Fig A.0.1 Conventional spiral inductor**

The usual LC sensor design is constructed from the spiral inductor placed around an interdigital capacitor [13-15]. However, for this traditional inductor as shown in Fig. A.1, there is a major drawback is that if the inductive structure is realized as a square spiral inductor it is necessary to have one underpass or overpass conductor for connecting the inner terminal to the outer contact. This requires the soldering one extra wire or adding another layer of a conductor [16] and consequently complicates the fabrication process and increases the production costs of the sensor. Furthermore, if this overpass is implemented with a discrete wire, smooth and good contact between the sensor and the building material is difficult (or almost impossible) and it can be a problem during measurement. Therefore, as our design, a completely new approach to design passive wireless sensors consisting of multi-wire coils which has parallel-connection structure is presented as shown in Fig A.2.

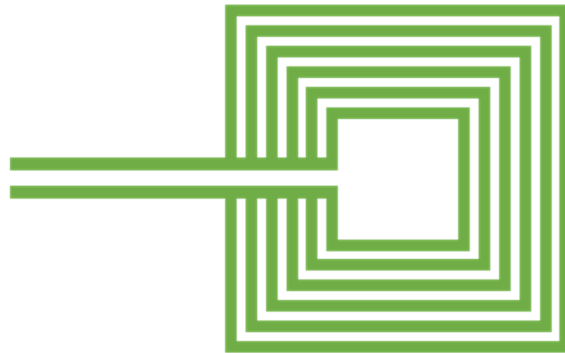


**Fig A.0.2 Layout of multi turns square planar inductor**

For a given shape, a planar inductor is completely specified by the number of turns  $N$ , the track width  $b$ , the spacing  $d$ , and any of the following: the outer diameter  $a(l)$ , the thickness of the track

t is ignored for their ignorable influence on the inductance. However, this thickness can't be neglected for the calculation of the self-resistance ( $R_L$ ) and the quality factor (Q).

The entire inductance of the parallel wires is calculated using Eq. (A.1).

$$L_{coil} = \frac{1}{\sum_{i=1}^{npw} L_{wire,i}^{-1}} \quad (A.1)$$

In general the inductance of a wire  $i$ ,  $L_{wire,i}$  is given by the sum of self-inductance  $L_{s,i}$  of mutual inductance  $L_{m,i}$  (see equation (4.14)).

$$L_{wire,i} = L_{s,i} + L_{m,i} \quad (A.2)$$

It is noticed that mutual inductance occurs between every two coils closed to each other. Obviously, self-inductance is always positive in contrast with mutual inductance which depends on the direction of current. The same direction will increase inductance, vice versa. In our model, there is supposed to be a strong mutual inductance due to a large number of wires conducting current in one direction.

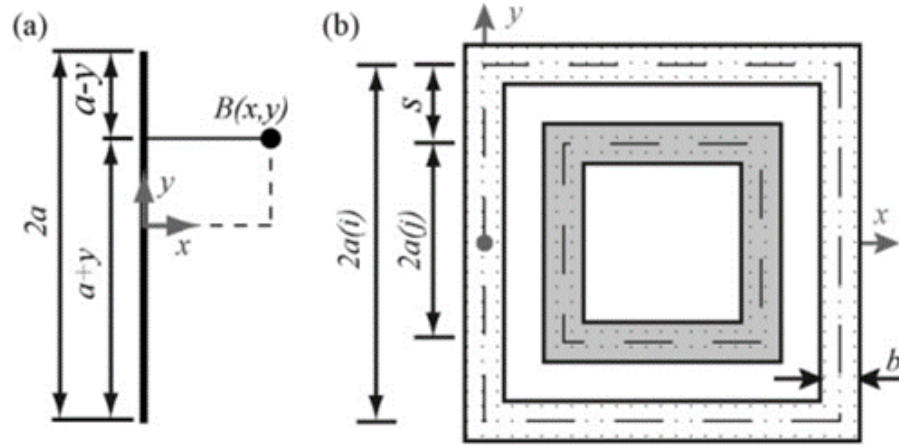


**Fig A.0.3 (a) Magnetic flux density  $B$  at point  $(x, y)$  arising from a current  $I$  and (b) Coil with two turns [48].**

Aiming at our model, the algorithm which will be presented below is based on Biot-Savart's law [48, 49]. Using Biot-Savart's law the magnetic flux density  $B$  at a point  $(x, y)$  arising from a current  $I$ , as shown in Fig 4.3, can be obtained by Eq. (A.3).

$$B(x, y) = \frac{\mu_1}{4\pi x} \left( \frac{a+y}{\sqrt{(a+y)^2+x^2}} + \frac{a-y}{\sqrt{(a-y)^2+x^2}} \right) \quad (\text{A.3})$$

Where  $a$ ,  $x$  and  $y$  are the half-length of the wire and the distance from the center point of the wire as shown in Fig A.3 (a). Since that the magnetic turns are surrounded by air in absent of magnetic corn,  $\mu$  is called vacuum permeability which has a value of  $4\pi \times 10^{-7}$  H/m. The magnetic flux  $\phi$  through an area, resulting from this flux density, is double integral over this area [50].

$$B(x, y) = \iint B(x, y) dx dy \quad (\text{A.4})$$

$$L = \frac{\phi}{I} \quad (\text{A.5})$$

This method has been established on the basis of a discussion of the magnetic flux density distribution. As the definition of magnetic flux and inductance, we can substitute basic equation (4. 16), (4. 17) in to (4. 15), obtain a reasonable equation below:

$$L = \frac{\mu}{4\pi} \iint \frac{1}{x} \left( \frac{a+y}{\sqrt{(a+y)^2+x^2}} + \frac{a-y}{\sqrt{(a-y)^2+x^2}} \right) dx dy \quad (A.6)$$

The inductance of wire segment can be obtain using equation (A.6) with some proper integration boundaries. In order to reduce the tedious calculate process and clarify the principle of compute, we simply our model into a rectangular shape with two turns, as indicated in Fig A.3 (b).

### *A.1.1 Self Inductance*

The self-inductance  $L_s$  of the entire outer rectangle as shown in Fig. A.3 (b) with a wire width  $b$  side length  $2a(i)$  is given by the following equation [50]:

$$L_{s,i} = 4 * \frac{\mu}{4\pi} \int_{-a(i)}^{a(i)} \int_{b/4}^{2a(i)} B(x, y) dx dy \quad (A.7)$$

It is noted that the lower integration boundary in  $x$  direction is  $b/4$  rather than 0. A detail derivation source value of  $b/4$  can be presented in [51]. Hence, the expression of integration which evolves from Eq. (A.6) using those integration boundaries is obtained below:

$$L_{s,i} = \frac{\mu}{2\pi} (b - b * \sqrt{\left(\frac{8a(i)}{b}\right)^2 + 1} + 8a(i) \left(-0.467 + \log\left(\frac{8a(i)}{b} + \sqrt{\left(\frac{8a(i)}{b}\right)^2 + 1}\right)\right)) \quad (\text{A.8})$$

Since that it is too cumbersome to calculate the equation above. In most case, we can simplify it into an empirical estimate. For the most practical planar inductor, these conversions can be verified:

$$\sqrt{\left(8 * \frac{a(i)}{b}\right)^2 + 1} \simeq \frac{8*a(i)}{b} \quad (\text{A.9})$$

$$\ln\left(\frac{4*a(i)}{b}\right) \gg \frac{b}{8*a(i)} - 0.08 \quad (\text{A.10})$$

Therefore,

$$L_{s,i} = \frac{4*\mu*a(i)}{\pi} * \ln\left(\frac{4*a(i)}{b}\right) \quad (\text{A.11})$$

As described by Dr. Arun Balakrishnan in [48], where he made a comparison between the values of calculated and measured one-turn inductance in the absence of any magnetic core material, it is indicated that the percent error goes up by the increasing of the ratio  $4*a(i)/b$ . Aiming at reducing the higher error, an effective method is given empirically:

$$L_{s,i} = \frac{4*\mu*a(i)}{\pi} * \ln\left(\frac{4*a(i)}{b} - 1\right) \quad (\text{A.12})$$

### *A.1.2 Mutual Inductance*

The expression for mutual inductance between every two wires can be deduced easily in the same way except that integration boundaries should be modified.

$$L_{m,i-j} = 4 * \frac{\mu}{4\pi} \int_{-a(i)}^{a(i)} \int_{a(i)-a(j)}^{a(i)+a(j)} B(x, y) dx dy \quad (\text{A.13})$$

Obviously, we can also work out the exact expression for mutual inductance using substituting method, as shown in equation (A.14).

$$\begin{aligned} L_{m,i-j} = & \frac{2\pi}{\mu} * (-a(i)(2 \operatorname{arcsinh}(1) - 2^{\frac{3}{2}} + \log(a(i) - a(j)) + \log(a(i) + a(j)) + \log(a(j) - a(i) + \\ & \sqrt{2a(i)^2 + 2a(j)^2}) - \log(a(i) + a(j) + \sqrt{2a(i)^2 + 2a(j)^2}) - \log(\sqrt{2a(i)^2 + a(j)^2 + 2a(i)a(j)} - \\ & a(i)) - \log(\sqrt{2a(i)^2 + a(j)^2 + 2a(i)a(j)} + a(i)) - a(j) \left( \log\left(\frac{a(i)-a(j)+\sqrt{2a(i)^2+2a(j)^2}}{a(i)^2-a(j)^2}\right) + \right. \\ & \left. 2 \log(a(i) - a(j)) - \log(a(i) + a(j) + \sqrt{2a(i)^2 + 2a(j)^2}) \right) - 2\sqrt{2a(i)^2 + 2a(j)^2} \end{aligned} \quad (\text{A.14})$$

As discussed above, a simple expression for the mutual inductance can be empirically derived in a same way, as shown by Eq. (A.27)

$$L_{m,i-j} = \frac{2*\mu}{\pi} * 2 * a(j) * (0.9 * \ln\left(\frac{a(i)+a(j)}{a(i)-a(j)}\right) - 0.37 * \ln\left(\frac{a(j)}{a(i)}\right) - 0.025) \quad (\text{A.15})$$

### A.1.3 Algorithm for Multi-wire Coils

To calculate the entire inductance of a coil, the self-inductance of each wire and the mutual inductance between this wire and any other wire must be calculated. To simplify the algorithm the

numbering scheme shown in Fig. A.2 is used. The most outer wire has number 1, the next 2 and so on till the last number is equal to the product of the number of parallel wires (npw) and the number of turns. If the index “npw” is equal to one, only one wire exists. Using Eq. (A.2), we can calculate the whole inductance on the nth wires:

$$L_{m,i} = \sum_{j=1}^{j=i-1} L_{m,i-j} + \sum_{j=i+1}^{j=npw} L_{m,i-j} \quad (\text{A.16})$$

Substituting Eq. (A.12) and (A.16) into (A.2), then the entire inductance is the parallel connection of all wires as given by Eq. (A.3). It is noted that there exists an equation, as shown below, which must be satisfied by calculation procedure.

$$a(i) - a(j) = (j-i) * s \quad (4.29)$$

Where s is defined by the distance between center lines of two adjacent side as presented in Fig. A.3 (b).

## **A.2 Proof of Concept of the Antenna with Novel Configuration**

This analysis as part of the optimization of the sensor design, plays an essential role in optimizing the design of inductor which not only is a component comprising LC resonant circuit with capacitor resulting converting the change of capacitance to relative frequency shift, but also takes position as power receiver through inducting oscillating magnetic field sent out by read

antenna by way of process known as coupling. This work helps understand the frequency response of this antenna configuration in order to improve the optimization of the sensor design (Fig. A.4).



**Fig A.0.4 Parallel square shape antenna configuration**

Based on this parallel- configuration, we setup an experiment as illustrated in previous section shown Fig. 5.8 but apply antenna with this specific shape, of which the aim is explore the influence caused by number of wire turns for inductance value.

The frequency- impedance graphs with different antenna turns are obtained by experiment indicated in Fig. A.5-A.8 and several related coefficients are demonstrated, such as peak value, bandwidth and amplitude.

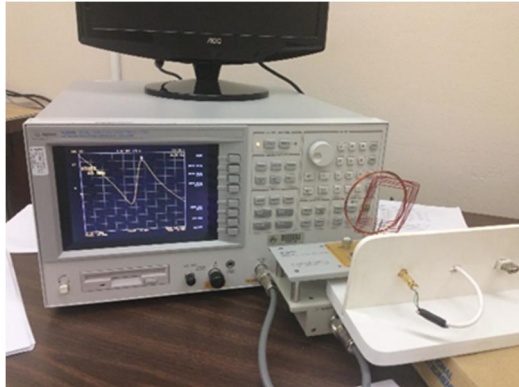


**Fig A.0.5 Experiment setup with seven coil turns**

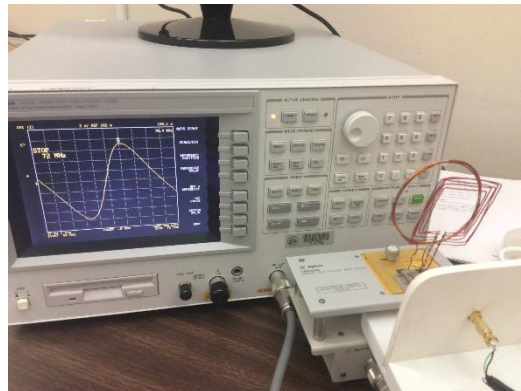


**Fig A.0.6 Experiment setup with five coil turns**

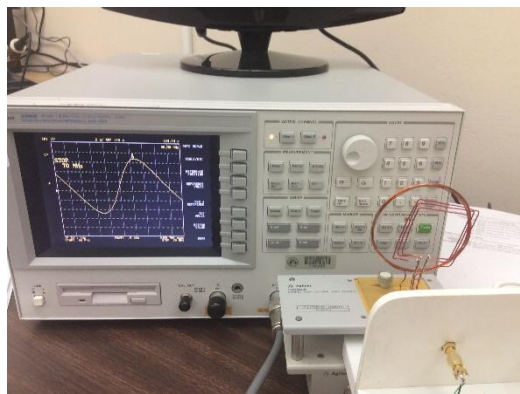


**Fig A.0.7 Experiment setup with three coil turns**

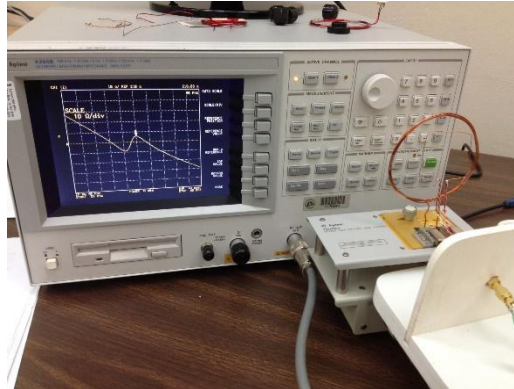


**Fig A.0.8 Experiment setup with one coil turns**

According to Fig. A.6, a plot indicating the relationship between number of coil turns and peak value, as well as impedance amplitude is shown below. Close inspect Fig. A.7, we can include obviously peak value which equals to resonant frequency will be increasing by the increase of inductance turns, meanwhile impedance amplitude, on behalf of somewhat signal strength, also has rising trend.

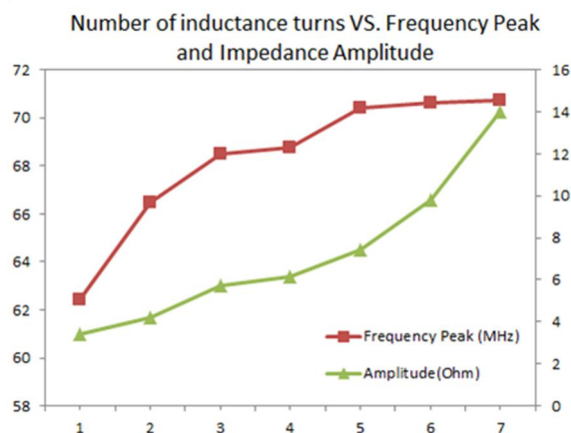


**Fig A.0.9 Number of inductance turns VS. Frequency Peak and Impedance Amplitude**

On other hand, the resistance has a major effect on one of our target- Q factor which is used to evaluate the quality of proposed LC circuit. Higher Q indicates a lower rate of energy loss relative present to the stored energy of the resonator; the oscillations die out more slowly. As usual, Q-factor is used to characterize a resonator bandwidth relative to its center frequency, which means the higher the Q, the narrower and 'sharper' the peak is.

In our case, due to this specific configuration, the total resistance of the whole inductor would be less than any one of each coil. As a result, higher Q factor meets our primary design demand.

### **A.3 Conclusions**

In this chapter, the alternative configuration of the inductor is introduced. In order to valid the fact that the inductor with novel configuration can be used to replace conventional spiral planar coil for combination of proposed LC circuit with interdigital capacitor, the proof of concept test was performed. As we expected, this novel inductor with parallel-square sharp can play a role as a inductive component for signal transmission so that the frequency response in impedance plot, especially resonant frequency shift resulting from the turns of antenna, can be detected. For calculation of total inductance, our design, combining with a lot of literatures [48, 49, 50, 51], has some innovative results. Consequently, this proposed novel antenna may broaden the area of planar inductor further.

## **Appendix B. Sensor Fabrication**

Based on sensing analysis, inductive power and entire sensor design consideration, in this appendix we will discuss sensor fabrication using fabricating microelectromechanical system (MEMS) technique. For the fabrication of the interdigital sensor, we will use the photolithography process which is one of the most important approaches in bulk micromachining. Photolithography is a process used in micro-fabrication to selectively remove parts of a thin film. It uses light to transfer a geometric pattern from a photomask to a light-sensitive chemical (photoresist) on the substrate. A series of chemical treatments then engraves the exposure pattern into the material underneath the photoresist. This process was made at Conte Nanotechnology Cleanroom Lab at University of Massachusetts (UMass) at Amherst in collaboration with the Center for Hierarchical Manufacturing, an NSF Nanoscale Science and Engineering Center (NSEC). In order to make the whole project coherent throughout, the fabrication process of sensor is briefly described as further reference.

### **B.1 Pattern Design**

Based on the considerations on design of interdigital circuit discussed in previous chapter, the sensor prototype patterns are designed in Draftsight<sup>®</sup> and Eagle<sup>®</sup> as shown in Fig. B.1.

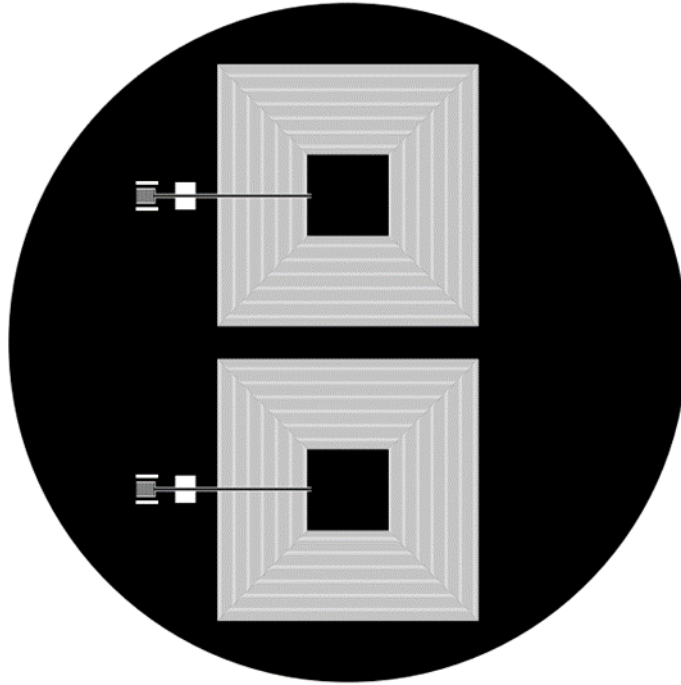


**Fig B.0.1 Two chips on top of silicon wafer substrate**

The planar inductor with seventy turns was made with 0.15mm width and 0.04mm gap between adjacent tracks is connected to the electrodes of the capacitor with same parameters as model ② we discussed in last chapter. Fig. B.1 presents the optimal design based on overall consideration and geometric parameters is shown in Table B.1.

**Table B.0.1 Fabrication parameter**

PARAMETER	SYMBOL	PDMS
Finger Width of Capacitor	$W_C$	0.01mm
Finger Gaps of Capacitor	$G_C$	0.01mm
Finger Length of Capacitor	$L_C$	2mm
Number of Finger	$N_C$	130
Coil Width of Inductor	$W_L$	0.15mm
Coil Gaps of Inductor	$G_L$	0.04mm
Outer radius of Inductor	$R_O$	19.115mm
Inter radius of Inductor	$R_I$	6.005mm
Number of Coil	$N_L$	70

## **B.2 Fabrication Procedure**

The basic procedure for Photolithography is briefly outlined in below:

1. Cleaning. The wafer surface is cleaned with a solvent to drive off organic or inorganic contaminants which usually removed by wet chemical treatment, such as RCA clean [41] based on solutions containing hydrogen peroxide. Surface condition would offer a better contact for the applied photo resist (PR) and provide a good circuit condition.
2. Preparation. Firstly, the wafer should be heated to a temperature sufficient to remove any moisture that may be present on the wafer surface. Then introduce an “adhesion

- promoter”, such as hexamethyldisilazane (HMDS) to promote adhesion of the photoresist to the wafer resulting in a highly water repellent layer. Finally, apply a thin layer of Photoresist on the surface of the wafer and make it spread all over the surface instead of just dropped on one point on the surface. In order to get a uniform thin layer, a spin coating which typically runs at 1200 to 4800 RPM for 30 to 60 seconds is used.
3. Exposure. A transparent photographic film which contains the pattern of the desired circuit is aligned on the prebaked wafer. Then the photoresist is exposed to a pattern of intense light, which causes a chemical change that allows some of the photoresist to be removed by a special solution, called "developer" by analogy with photographic developer. In terms of our task, negative photoresist is applied, so that unexposed regions are soluble in the developer.
  4. Developing. Before developing, a post-exposure bake (PEB) is performed typically to help reduce standing wave phenomena caused by the destructive and constructive interference patterns of the incident light. Then, remove the mask pattern film and replace the wafer into the developer solvent. Hold the wafer with tweezers and agitate mildly until the PR which is expose to the UV light has been fully dissolved.
  5. Etching. Leave the wafer into the hard baking oven at 120 for 60 minutes. Cool it and immerse it into the solutions of a board etchant. Hold the clad with tweezers and agitate mildly until the copper, which is not covered by the hard-baked PR, is completely etched away.
  6. Photoresist removal. A liquid called “resist stripper” should be utilized to remove the residual photoresist from the substrate surface.

Major procedures are briefly shown below in Figure B.2.

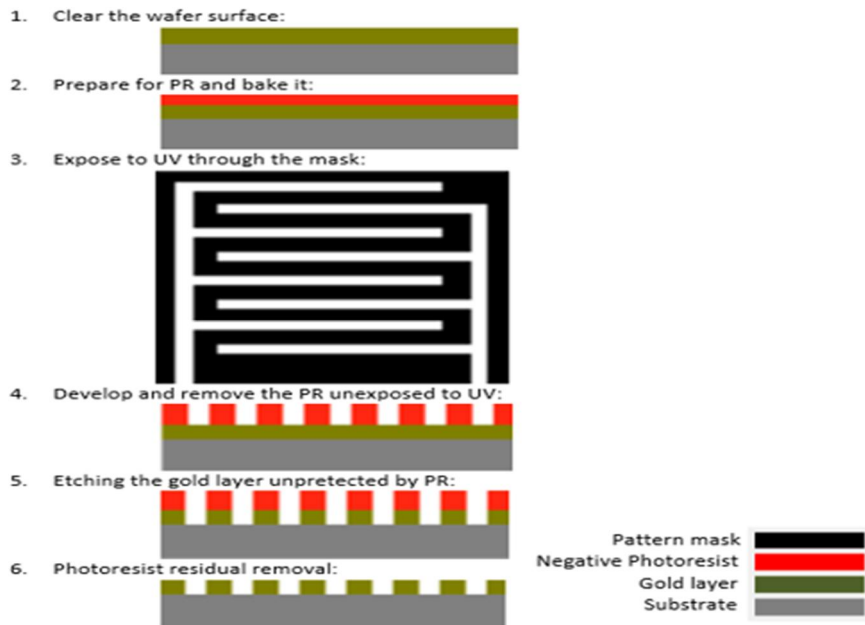


**Fig B.0.2 Sensor fabrication procedure**

Fabricated sensors are shown below as Fig. B.3

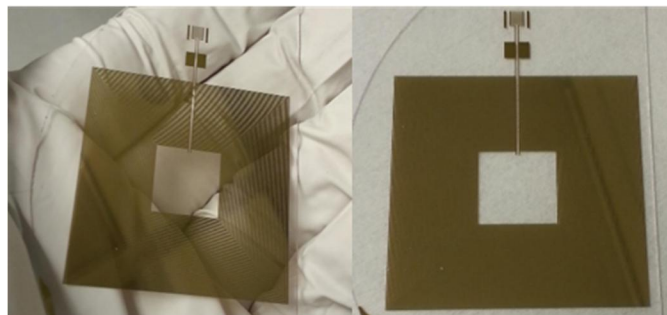


**Fig B.0.3 Fabricated sensor prototype**